TAMPERE UNIVERSITY OF TECHNOLOGY

TIZIANA ZEDDA

CONSTRUCTION AND TESTING OF A POSITRON EMISSION TOMOGRAPHY DEMONSTRATOR

Master of Science Thesis

Examiners: Prof. Ulla Ruotsalainen
PhD Viivi Nuottajärvi
Prof. Viviana Fanti

Examiners and topic accepted by the Faculty council on 3rd April 2013

Ot Anaizit, esuaceb uoy reven evag pu.

CONTENTS

Abstract xiii
Preface xv
1. Introduction 1
2. PET basics and development 3
2.1 The Physics of PET 3
2.1.1 The PET camera 3
2.1.2 Annihilation 4
2.1.3 Solid Scintillators 6
2.1.4 Photodetector 8
2.1.5 New PET camera design 11
3. Methods 15
3.1 Scintillating crystal bars 15
3.2 Wavelength Shifting strips 16
3.3 Photodetectors 17
3.4 Readout Electronics and data acquisition 19
3.5 Mechanical Assembly 22
4. Experimental set-up and measurements 25
4.1 Intrinsic radioactivity of LYSO 25
4.2 Photoelectric peak of 511 keV photons 27
5. Data analysis and results 31
5.1 Intrinsic radioactivity of LYSO 31
5.2 Photoelectric peak of 511 keV photons 33
5.3 Energy calibration 34
5.4 Energy resolution 39
6. Conclusions and outlook 41
Bibliography 45

LIST OF SYMBOLS AND ABBREVIATIONS

PET	Positron Emission Tomography	xiii
WLS	Wavelength Shifter	xiii
$MATLAB$	Matrix Laboratory	xiii
$SPECT$	Single-photon Emission Computed Tomography	1
CT	X-ray Computed Tomography	1
MRI	Magnetic Resonance Imaging	1
TOF	Time of flight	1
SNR	Signal to Noise Ratio	2
DOI	Depth of Interaction	2
PMT	Photomultiplier Tube	4
β^+	Beta plus decay	5
P	Proton	5
N	Neutron	5
ν	Neutrino	5
e^+	Positron	5
γ	Gamma photon	??
$1/\mu$	Attenuation Length	7
ρ	Density	7
Z_eff	Effective atomic number	7
$\Delta E/E$	Energy resolution	7
$NaI(Tl)$	Sodium Iodide doped with Thallium	7
BGO	Bismuth Germanate	7
LSO	Lutetium Oxyorthosilicate doped with Cerium	7
GSO	Gadolinium Oxyorthosilicate doped with Cerium	7
BaF_2	Barium Fuoride	7
$LYSO$	Cerium doped Lutetium Oxyorthosilicate	7
μ	Linear attenuation coefficient	8
μ/ρ	Mass attenuation coefficient	8
λ	Wavelength	8
APD	Avalanche Photo Diode	9
FOV	Field of View	11
Z	Coordinate	11
Y	Coordinate	12
X	Coordinate	12
$\sigma_{x,y}$	Digital resolution	12
d	Dimension	12
$G-APD$	Geiger mode Avalanche Photo Diode	15
^{176}Lu	Lutetium 176	15
β^-	Beta minus decay	15

^{176}Hf	Hafnium 176	15
$PTFE$	Teflon	15
PVL	Polyvinyltouluene	16
ESR	Enhanced Spectacular Reflector	16
$MPPC$	Multi-pixel Photon Counter	17
PDE	Photon Detection Efficiency	19
DSP	Digital Signal Processor	19
$P3$	Pipelined Parallel Processor	20
ADC	Analog-to-Digital Converter	21
SMB	Server Message Block	21
^{68}Ge	Germanium 68	27
^{68}Ga	Gallium 68	27
α	Parameter	32
β	Parameter	32
δ	Parameter	32
R^2	Coefficient of correlation	32
Q	Collected charge	32
α'	Parameter	33
β'	Parameter	33
δ'	Parameter	33
E	Energy of the photon	35
a_1	Parameter	36
b_1	Parameter	36
c_1	Parameter	36
p_0	Parameter	37
p_1	Parameter	37
p_2	Parameter	37
a_2	Parameter	38
b_2	Parameter	38
c_2	Parameter	**??**
R	Energy resolution	39
$FWHM$	Full Width at Half Maximum	39
X_0	Amplitude of the peak	39
σ	Standard deviation	39

LIST OF FIGURES

2.1 Schematic view of PET functioning [10] (modified). 4
2.2 Diagram of basic components of a PET detector. 4
2.3 The process of positron emission and following positron-electron annihilation. 5
2.4 Scheme of the energy levels in a scintillator crystal and the mechanism of the emission of a photon by scintillation, after absorption of a γ ray. 6
2.5 A scheme of a scintillator coupled to a photomultiplier, showing the photocathode on the left, the dynodes in the middle, the anode on the right end, and showing the production of an electrical pulse from a photon. 9
2.6 a) Cross-section of an APD. b) Representation of the principle of the avalanche production of e-h pairs in Geiger mode. 10
2.7 a)Radial orientation of the detectors inside a classical PET b) Axial orientation of the detectors for the new concept of PET [10]. 12
2.8 Principle of the light propagation and principle of the axial coordinate readout using scintillating crystals and WLS strips [5] 12

3.1 a) Beta distributions of a single crystal (1" diameter by 1" long) of PreLude^{TM} 420 b) Emission spectrum of PreLude^{TM} 420 [21]. 16
3.2 The WLS emission spectrum [11]. 17
3.3 The MPPC detection efficiency as a function of the wavelength of the incident light (at 25℃) [13]. *Photon detection efficiency includes effects of crosstalk and after pulses. 18
3.4 The circuit for biasing the MPPCs. 18
3.5 64 channels functional block scheme of the acquisition module, implemented in the IQSP582 Data Acquisition System [23]. 20
3.6 Sketch of the configuration of the electronic chain. 22
3.7 Assembling of the crystals and the WLS inside one Avantomography module. 23
3.8 The Avantomography demonstrator. 24

4.1 Set-up for the measurement of the intrinsic radioactivity of the LYSO. The 20 LYSO bars are placed all together forming one bloc inside a dark-room box. The selected crystal is the only one connected to the acquisition system in the sketch. 26
4.2 Charge spectrum of the intrinsic radioactivity of one LYSO crystal. . 27
4.3 Set-up for the measurement of 511 keV photoelectric peak of a ^{68}Ge/^{68}Ga radioactive source. The source is placed in the center of the (FOV) of the device as visible in the picture. 28

4.4 Sketch of the experimental set-up. The source is placed in the center of the (FOV). The radioactive part goes 8 cm below the center and 8 cm above, irradiating equally the 4 modules. 28
4.5 Charge histogram of 511 keV photons detected in LYSO crystal channel 1. 29

5.1 Charge spectrum of the intrinsic radioactivity of one LYSO crystal, with a Gaussian fit for each peak. 32
5.2 Charge spectrum of the 511 keV photons detected in one LYSO crystal, with a Gaussian fit for the photoelectric peak. 34
5.3 Linear fitting for the three LYSO peaks. The photoelectric peak at 511 keV is below this line because of the non linear response of the MPPC at high energies. 36
5.4 Energy calibration curve of one of the LYSO crystals (continuous line), which deviates from the linear fitting of the three LYSO peaks (dashed line). 37
5.5 Spectrum of the 511 keV photons detected in one LYSO crystal, with a Gaussian fit for the photoelectric peak, in energy scale. 38

LIST OF TABLES

2.1 Physical properties of scintillators used in PET. The energy resolution and attenuation coefficients (linear μ and mass μ/ρ are measured at 511 keV) [8]. 8

3.1 Properties of the LYSO crystal used in Avantomography demonstrator [21]. 16
3.2 Properties of the WLS strips used in Avantomography demonstrator [11]. 17
3.3 Properties of the MPPC used in Avantomography demonstrator [13]. 18
3.4 Specifications of the PhotoniQ 64 channel data acquisition system used in the Avantomography demonstrator [24]. 21
3.5 Specifications of a single 32 channels SMB distribution system [25]. . 21

4.1 Settings applied to the demonstrator for the acquisition of the LYSO intrinsic radioactivity. 27
4.2 Settings applied for the acquisition of the charge spectrum of 511 keV photons. 29

5.1 Parameters of the Gaussian fit curves. The parameter α is the height of the peak of the curve, β is the position of the centre of the peak, δ is the standard deviation, and R^2 is the correlation coefficient. 32
5.2 Peak position and relative energy. 33
5.3 Parameters of the Gaussian fit curve for the photoelectric peak. The parameter α' is the height of the peak of the curve, β' is the position of the centre of the peak, δ' is the standard deviation and R^2 is the coefficient of correlation between the fitting curve and the data. . . . 34
5.4 Peak position and relative energy. 35
5.5 Peak position, relative energy and relative error (standard deviation) of the LYSO intrinsic radioactivity and the annihilation photons. . . . 35
5.6 Values of the parameteres of the 3-parametrized fitting function. The parameter b_1 is negative, because it describes the decreasing trend of the exponential fitting curve. 36
5.7 Parameters of the Gaussian fit curve for the photoelectric peak, converted in energy scale. The parameter a_2 is the height of the peak of the curve, b_2 is the position of the centre of the peak, and c_2 is the standard deviation and R^2 is the correlation coefficient. 38

ABSTRACT

TAMPERE UNIVERSITY OF TECHNOLOGY
Master's Degree Programme in Physics
TIZIANA ZEDDA : Construction and testing of a Positron Emission Tomography demonstrator
Master of Science Thesis, x pages, x enclosure pages
March 2013
Major: Physics
Examiners: Ulla Ruotsalainen, Viivi Nuottajärvi
Supervisor: Viviana Fanti
Keywords: Positron Emission Tomography, PET, energy calibration, energy range, energy resolution, scintillating crystals, LYSO, wavelength shifter, WLS, MPPC, intrinsic radioactivity, 511 kev

In this thesis we present the Avantomography demonstrator, which is being implemented and tested at Tampere University of Technology (Tampere, Finland). We also describe the first tests performed with it and the obtained results. The final aim of this master thesis is the energy calibration of the scintillating crystals and the electronic chain for data acquisition.
This new small Positron Emission Tomography (PET) demonstrator follows the recent innovations presented by the AX-PET group [5], at CERN. This is the first functioning version of a prototype of a light and compact PET scanner. The novel geometry, used to build the Avantomography demonstrator, is based on scintillating crystals and wavelength shifting (WLS) plastic strips, allowing high resolution and high sensitivity at the same time. The device consists in two small and compact modules, with two different adjustable parts inside. Each detector module is built up from long scintillator bars placed in the trans-axial plane and orthogonal WLS strip arrays. Preliminary tests with a standard positron emitter source has been performed in order to test the acquisition chain and to calibrate the demonstrator. First test has been performed measuring the intrinsic radioactivity of the scintillating crystals. For a complete calibration of one crystal, a test with a linear positron emitter source has been performed at the Tampere University Hospital (Tampere, Finland). From these measurements the spectra of different energy peaks are acquired and plotted. Using a dedicate MATLAB code, different Gaussian fits are calculated to find the position of each peak. With these values a 3-parameters fitting curve has been evaluated in order to obtain the non linear curve for the energy calibration. Furthermore a first evaluation of the energy resolution has been calculated starting from the acquired data. With its compact and light geometry, high resolution and high sensitivity this detector has a promising layout as a preclinical

PET scanner.

PREFACE

I would like to express my gratitude to my professors and reviewers: Prof. Ulla Ruotsalainen and Prof. Viviana Fanti. They gave me the opportunity to work on my thesis at the Tampere University of Technology with their invaluable support and help. A deep thanks to Viivi Nuottajärvi, whose guidance during the job for my thesis in Finland made the fulfillment of my work possible. Physics could be frustrating, but working with her was an amazing and even funny experience. A sincere thanks to Prof. Karri Palovuori and Antti Nuottajärvi for the significant technical support.
I am also grateful to all the new friends I have met in Tampere. With them I had unforgettable experiences, a lot of fun and sincere support and help during my work for the thesis. Thanks to them (especially Michal) I felt in love with Finland. I am also truly indebted to my colleagues and friends at Universitá di Cagliari, who shared with me the joys and frustration of studying and loving physics. Thanks to all of my friends in Italy and abroad, they gave me so much love that I have never felt away from home. Moreover a special thanks to Piccardo.
Finally a strong and loving thanks to my family. They always gave me their support no matter what happened in my life. I deeply love them even if I am far from home and I would not be the person I am now without their guidance and their love. Thanks to Marzia, she is not just a sister, but an ally too.

Tampere, March 2013
Tiziana Zedda

1. INTRODUCTION

The origin of nuclear medicine can be traced back to the last year of the 19th century with the discovery of the radioactivity by Henri Becquerel (1896), of the radium by Marie Curie and the discovery of the x-rays by Wilhelm Roentgen (1895) [22]. Both x-rays and radium sources were quickly adopted for medical application and were used to make shadows images in which the radiation was transmitted through a body on a photographic plate. It was possible for the first time to see "inside" the human body noninvasively. Although x-rays soon became the method for producing "radiographs", nuclear medicine needed further developments. The first human study employing radioactive tracers was made by Blumgart and Weiss (1927). An aqueous solution of radon was injected intravenously and the transit time of the blood from one arm to the other was measured, using a cloud chamber as radiation detector. The invention of the cyclotron in the 1930s (Lawrence) started the production of new artificial radionuclides, extending the range of biologic processes that could be studied. The development of new technologies in 1950s allowed to obtain images of the distribution of radionuclides inside the human body rather than just counting the activity in few small points. In 1951 for the first time a positron emitter was used for imaging by Wrenn and co-workers. The final important development was the mathematics for reconstruction of tomographic images, from a set of different angular views around a human body. With that it was finally possible to create a true three-dimensional representation of the radioactivity distribution inside a human body. This allowed the development of Positron Emission Tomography or PET (Phelps and colleagues) and Single-photon emission computed tomography or SPECT (Kuhl and colleauges) during the 1970s and started the modern era of nuclear medicine.

Nuclear medicine is nowadays used for a lot of different types of diagnostic tests and covers the major organ systems in a body. In 2008 there were more than 3000 PET scanners installed in the world, performing 4 million of procedures every year [22]. The development of positron emission tomography has resulted in a wide variety of scanner designs over the years. Almost all PET scanners are now integrated with a CT scanner in a system that gives better diagnostic insight, thanks to the combination of structural (CT) and functional (PET) imaging. New imaging modality are quickly developing, for example in 2011 first commercial PET/MRI systems were being delivered [22]. A new type of commercial PET is the Time-of-flight (TOF) camera, where the arrival time difference of the photons is used to further restrict

the position. These systems are developed with the goal of improving the signal-to-noise ratio (SNR) in the reconstructed images and reducing the random coincidence event rates [15]. The genetic research and the pharmaceutical industry require small animal PET scanners with very demanding high performances in terms of spatial resolution. This feature is well established in human PET, but the challenge for small animal PET is to achieve the same quality standards in volumes which are orders of magnitude smaller. New cameras with a detector system that provides Depth of Interaction (DOI) information can get a uniform resolution and coincidence sensitivity, allowing to use smaller ring diameters[17]. Research is going on in order to surpass the limits of existing scanners. Examples are the Crystal Clear Collaboration [14], and the recent AX-PET at CERN [5].

2. PET BASICS AND DEVELOPMENT

Medical imaging is a way of viewing anatomical structures and also physiological functions of a body. Nuclear medicine imaging is a technique based on the acquisition of the decay of radio-isotopes bound to molecules with specific biological properties, injected into the body. They are obtained by using equipment for planar scintigraphy, Single Photon Emission Computed Tomography (SPECT) and Positron Emission Tomography (PET) [22]. In a scintigraphy and a SPECT scan, single γ photons are emitted and detected with a gamma camera. These camera consists of a lead collimator to get a linear propagation of the photons, a crystal scintillator to convert γ rays to visible light and photomultiplier tubes associated to electronics, in order to convert light into an electrical signal [19]. Positron emission tomography (PET) is the newest method and uses positron emitting radioisotopes. It consists of a set of detectors that surround the patient and detect in coincidence the two gamma annihilation photons originated from a β^+ decay. PET and SPECT have physical and technical similarities, but PET has some advantages over SPECT. The most important is that the absence of a lead collimator permits to get a higher sensitivity [6]. The PET radionuclides include the body's main constituents (positron emitting isotopes of carbon, oxygen and fluorine) and give a wide variety of radio-pharmaceuticals, useful in research studies and clinical application. Most of PET investigations in medicine are in oncology (74% of the total), the remains are in cardiology (17%) and neurology (9%) [16].

2.1 The Physics of PET

2.1.1 The PET camera

A PET scanner is designed to detect and localize the simultaneous back-to-back annihilation photons and to convert this information into a measurable electrical signal. A Schematic view of PET functioning is shown in Figure 2.1

The subject is surrounded by a cylindrical ring of detectors, with a typical diameter of 70-100 cm and an axial extent of 10-20 cm. Detector blocks consist of scintillator crystals and photodetectors [19].

A good photon detector for PET scanner must have a very high *efficiency* for detecting 511 keV photons, that means a high number of photon pairs detected, in order to give a good signal-to-noise ratio. The detector also must give precise information on the location of the interaction, resulting in a good *spatial resolution* of the images.

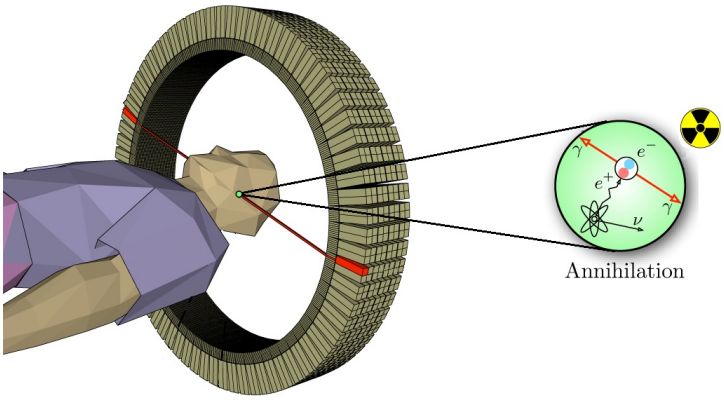

Figure 2.1: Schematic view of PET functioning [10] (modified).

A high spatial resolution can be achieved in two ways, either by using arrays of small elements, or by using large area detector with a position-sensing capability built in. Another important characteristic for a photon detector is the *time resolution*, which is the ability to determinate the time of arrival of the photons, with the aim to discriminate the pairs of annihilation photons; it is typically on the order of 2 to 6 ns. A typical time window used in PET scanner is usually two or three times the time resolution, in order to avoid the rejection of annihilation photon pairs, in the range of 4 to 18 ns. Finally the detector must have a high *energy resolution*, which is the ability to indicate the energy of the incoming photons such that the scattered photons can be rejected [6].
A photon detector for PET is typically made by a solid scintillating crystal for the detection of the γ rays, coupled to a light sensor such as a photomultiplier tube (PMT) or a photodiode, which absorbs the light emitted by the scintillator and produces an electrical signal. A scheme of its basic components is shown in Figure 2.2 and the properties of the most important parts will be described in the following sections.

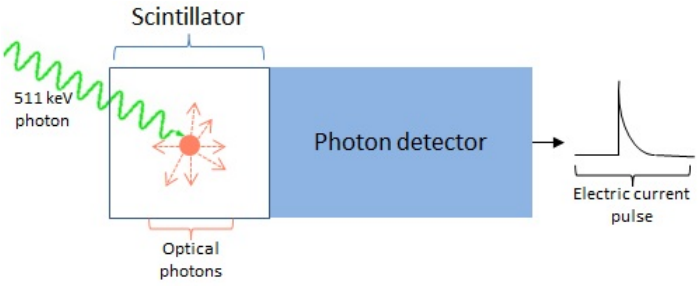

Figure 2.2: Diagram of basic components of a PET detector.

2.1.2 Annihilation

As said before PET imaging technique uses the unique decay characteristic of radionuclides that emit positrons.

A normal way by which nuclei with an excess of protons decay is the beta-plus decay (β^+). A proton (P) inside the nucleus of an atom is converted into a neutron (N), a neutrino (ν) and a positron (e^+)[6].

$$P \rightarrow N + e^+ + \nu \tag{2.1}$$

The net energy released during the emission is shared among the daughter nucleus, the neutrino and the positron.
The positron has a very short lifetime in most materials. It loses its kinetic energy by inelastic collisions with atomic electrons of the tissue, and once most of the energy is dissipated, an *annihilation* occurs between that and one electron of the material. Annihilation is a process where the mass of both the electron and the positron is converted into electromagnetic energy.

$$e^+ + e^- \rightarrow \gamma + \gamma \tag{2.2}$$

As the particles are almost at rest, the released energy comes largely from their mass in form of a pair of 511 keV of gamma rays (γ) which travel in opposite direction.

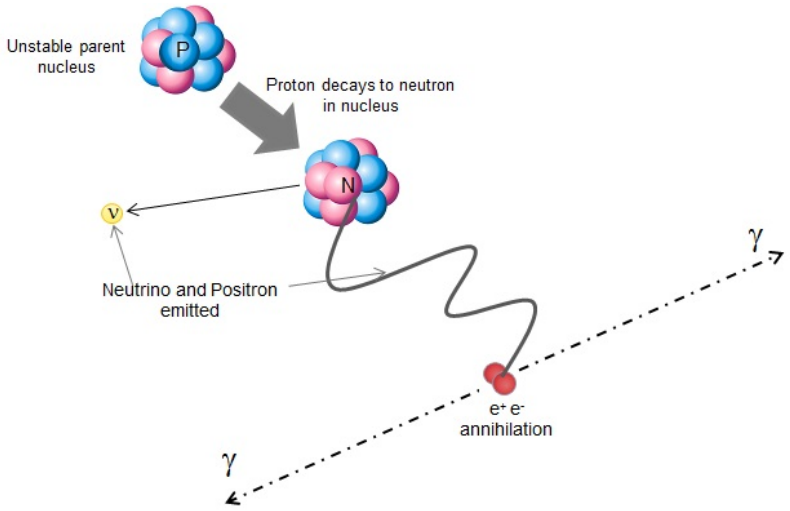

Figure 2.3: The process of positron emission and following positron-electron annihilation.

The annihilation process has very important advantages for PET imaging. First the produced γ rays are very energetic and have a very good chance of escaping the body and being detected outside. Furthermore the annihilation photons are emitted with a specific geometric relationship, if both of them are detected and localized externally, the line joining the detected locations passes directly through the point of annihilation. The site of annihilation is usually very close to the point of positron emission, so that it is possible to localize where the radio-pharmaceutical was absorbed.

2.1.3 Solid Scintillators

As mentioned before, the scintillation crystals are the most used detectors for 511 keV photons in PET, thanks to their high stopping power and energy resolution.
In certain types of materials, the energy deposited by an energetic particle can create excited atomic states that quickly decay through the emission of visible or ultraviolet light. This process is called *scintillation* and this type of materials are known as *scintillators*. The light is emitted isotropically and the amount of emitted photons is proportional to the amount of energy that is deposited inside the material. These materials can be organic or inorganic compounds and can be in both solid or liquid state [6]. In this thesis only solid state scintillators are described, because used in this job.
In a crystal lattice the outer electronic states of the atoms are disposed in a series of *allowed bands*. The bands within this series are separated by *forbidden bands*. The last filled band is called *valence band*, the first unfilled band is called *conduction band*. Electrons in valence band can absorb energy from the high-energy incident photon and get excited into the conduction band. Since this state is not as stable as the ground state, the electron de-excites by emitting scintillation photons and returns to the ground state. By adding few impurities to the pure crystal, some energy levels are created in the forbidden region, slightly above the valence band or slightly below the conduction one. This process minimizes the self-absorption of the scintillation photons by the crystals [8]. A schematic diagram of the process is shown in Figure 2.4.

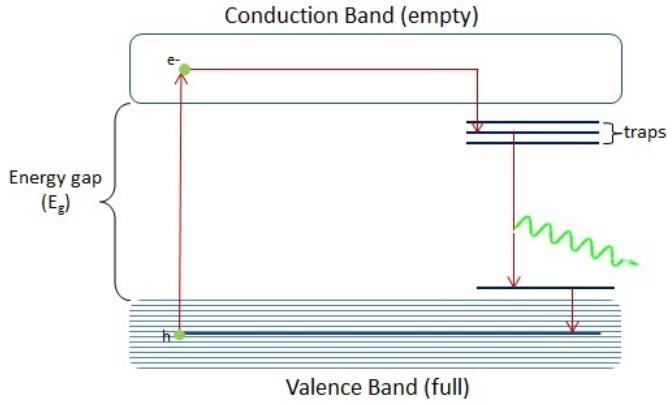

Figure 2.4: Scheme of the energy levels in a scintillator crystal and the mechanism of the emission of a photon by scintillation, after absorption of a γ ray.

For the purposes of the PET imaging the scintillator must have four important characteristics:

- high stopping power for 511 keV photons;
- short scintillation decay time;

- high light output per keV of photon energy;
- high intrinsic energy resolution.

The stopping power of a scintillator is characterized by the mean distance (attenuation length $1/\mu$) travelled by the photon before it deposits its energy by the interaction in the crystal [8]. The attenuation length depends on the density ρ and the effective atomic number (Z_{eff}) of the material. Best scintillators for PET are inorganic solid scintillators, because they have a short attenuation length, thus providing a high efficiency in stopping the γ photons [20].
The decay time determines the rate at which the light is emitted following the excitation. Decay times varies with the material and are typically in the range of nanoseconds (ns). As PET imaging involves the coincidence detection of the two annihilation photon, a short decay time assures a high efficiency in the discrimination of the events (reducing the number of random coincidence events occurring) [8].
The number of light photons produced per 511 keV interaction is important because the information is used in different ways. In many detectors the integrated light signal is used as a direct measure of the energy deposited in the scintillator and the relative amplitude of the signal coming from adjacent light sensors is used to determinate the location of the interaction [6]. Thereby a high light output scintillator helps to achieve a good spatial resolution and a good energy resolution.
The intrinsic energy resolution is affected by the inhomogeneities in the crystal structure as well as by the random variations in the direction of the light inside it. The energy resolution ($\Delta E/E$) of a PET detector depends on both the intrinsic energy resolution and the brightness of the scintillator.
Finally, the refraction index is also important because it determinates how efficiently the photons can be trasmitted from the scintillator to the photodetector. Large mismatches in the index result in significant internal reflection at the scintillator/detector boundary and reduce the trasmittion of the light to the photodetector.
The most used scintillators in PET are:

- sodium iodide doped with thallium NaI(Tl),
- bismuth germanate Bi_4 Ge_3 O_{12} (BGO),
- lutetium oxyorthosilicate doped with cerium Lu_2 SiO_5:Ce (LSO),
- yttrium oxyorthosilicate doped with cerium Y_2 SiO_5:Ce (YSO),
- gadolinium oxyorthosilicate doped with cerium Gd_2 SiO_5:Ce (GSO),
- barium fluoride (BaF_2)
- cerium doped lutetium oxyorthosilicate (LYSO).

Table 2.1: Physical properties of scintillators used in PET. The energy resolution and attenuation coefficients (linear μ and mass μ/ρ are measured at 511 keV) [8].

Property	NaI(Tl)	BGO	LSO	YSO	LYSO	GSO	BaF_2
Density (g/cm^3)	3.67	7.13	7.4	4.53	7.1	6.71	4.89
Effective Z	50.6	74.2	65.5	34.2		58.6	52.2
Attenuation length	2.88	1.05	1.16	2.58	12	1.43	2.2
Decay constant (ns)	230	300	40	70	41	60	0.6
Light output (photons/keV)	38	6	29	46	32	10	2
Relative light output (%)	100	15	75	118		25	5
Wavelength λ (nm)	410	480	420	420	420	440	220
Intrinsic$\Delta E/E$(%)	5.8	3.1	9.1	7.5	8.3	4.6	4.3
$\Delta E/E$(%)	6.6	10.2	10	12.5	10	8.5	11.4
Index of refraction	1.85	2.15	1.82	1.8	1.81	1.91	1.56
Hygroscopic?	Yes	No	No	No	No	No	No
Rugged?	No	Yes	Yes	Yes		No	Yes
$\mu(cm^{-1})$	0.3411	0.9496	0.8658	0.3875		0.6978	0.4545
$\mu/\rho(cm^2/gm)$	0.0948	0.1332	0.117	0.853		0.104	0.0929

Their properties are shown in Table 2.1.

Almost all PET scanners are today based on BGO crystal detecting arrays. They have the advantage of a high density, the highest known atomic number and high detection sensitivity. The main fault is the very high decay time, as shown in Table 2.1. A new generation of scanners based on faster crystals is now developing. New scintillating materials have been developed in the last 15 years, such of those from the family of Lutetium perovskites (LuAP), with similar properties of LSO (Lutetium orthosilicate). Other examples include LuAP:Ce, Y_2 SiO_5 (YSO), $LuBO_3$:Ce, and others based on lead (Pb), tungsten (W) and gadolinium (Gd).The LuAP has a high density (8.34 g/cm^3), a very short decay time (17 ns) but a very low brightness. Doped LSO's have interesting properties that varies in function of the number of Yttrium atoms which can replace some Lutetium atoms (LYSO crystals) [14]. LYSO has typically high light output, high density and an excellent timing resolution. The drawback of LYSO and other Lu-based scintillator materials, consists in the presence of intrinsic radioactivity ($\sim$300 counts$\cdot s^{-1}\cdot cm^{-3}$) due to the natural abundance (2.5%) of ^{176}Lu radioactive isotope (half life $\sim 2.2\cdot 10^{10}$ years) [7].

2.1.4 Photodetector

The photodetectors used in scintillation detection in PET can be divided into two categories, the photo-multiplier tubes (PMTs) and the semiconductor photodiodes (PD). Photo-multiplier tubes are the oldest and most used devices to measure and detect low levels of scintillation light [8].

The PM tube is a vacuum tube containing a photocathode at one end, the dynodes in the middle and an anode at the other end, as shown in Figure 2.5. A high voltage of $\sim$ 1000 V is applied between the photocathode and the anode, with an increment of $\sim$ 100 V between the dynodes, generating in this way an electric field between

the electrodes.

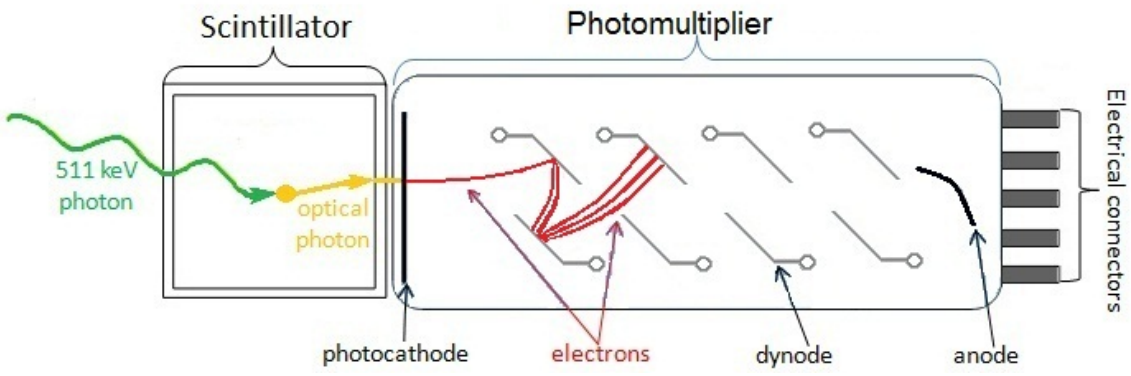

Figure 2.5: A scheme of a scintillator coupled to a photomultiplier, showing the photocathode on the left, the dynodes in the middle, the anode on the right end, and showing the production of an electrical pulse from a photon.

An incoming scintillation photon deposits its energy at the photocathode causing the emission of a photo-electron from it. In the presence of the electric field the electron accelerates to the first dynode and impacts on it, releasing more electrons. Each of these electrons is again accelerated to the next dynode and more electrons are again emitted. The process of multiplication continues until the last dynode is hit and in this way a pulse of electrons is produced, and is finally attracted to the anode. The pulse can be amplified, digitized and then delivered to a computer for the analysis [20]. The high gain obtained from a photo-multiplier tube leads to a very good signal-to-noise ration and is the first reason for the success of the PMT in PET.

Photodiodes, on the other hand are based on semiconductors, which have a high sensitivity for detecting scintillation photons. An important advantage of the solid state photodetectors is their immunity to magnetic fields which makes them suitable for the combination of PET and MRI. On the other hand, a significant disadvantage of the photodiodes is the very low signal-to-noise ratio due to the presence of thermally activated charge flows and very low intrinsic signal amplification. In recent years, a new type of photodiode has been developed, called Avalanche Photo Diode (APD), which has an internal amplification of the signal and can be used in PET also.
An APD is a variation of a p-n junction photodiode, it can reach a good internal amplification (10^6) when it works in Geiger mode [9]. When a p-n junction is reversely biased, an electric field exists in the proximity of the junction and keeps the electrons confined inside the n side and the holes inside the p side. When an incoming photon which sufficient energy is absorbed in the region where this field exists, an electron-hole pair can be created. Because of that field the electron drifts to the n side and the hole drifts to the p, producing in this way an electrical current. In an APD the amplitude of the electric field is very high, in this way when an electron-hole pair

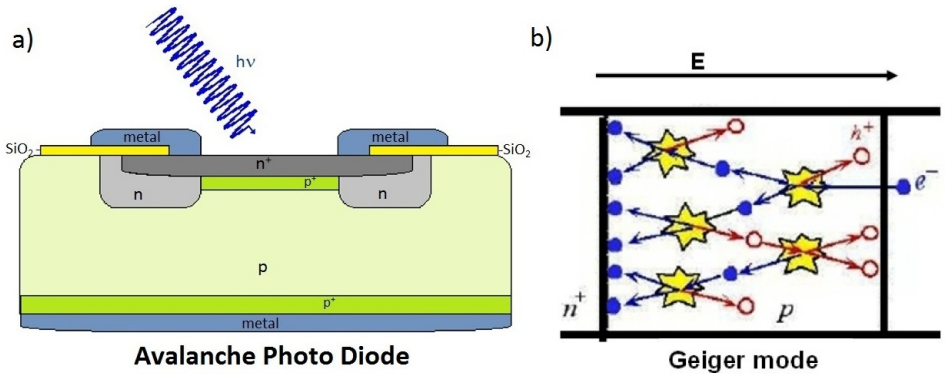

Figure 2.6: a) Cross-section of an APD. b) Representation of the principle of the avalanche production of e-h pairs in Geiger mode.

is generated, the electron (or the hole) accelerates and can gain sufficient energy from the field to generate another electron-hole pair, by collision with the crystal lattice. The new pair can again accelerate and create more electron-hole pairs, as an "avalanche". After some transition times a competition develops between the rate of creation of the pairs and the rate at which they are collected. If the magnitude of the reverse-bias voltage is below of the *breakdown voltage*, collection wins and the number of pairs declines. If the bias voltage is above the *breakdown voltage*, the pairs multiplication is faster on average than their extraction. In this condition the APD works in the so called *Geiger mode*. The more above the breakdown voltage the APD is biased, the faster is the production of pairs and the higher is the intrinsic gain ($10^5 - 10^6$). If there are resistances in series in the diode, more voltage drops across these resistance, as the current grows. This effect reduces the voltage drop and slows down the growth of the avalanche. Finally a steady-state is reached between the generation and the extraction rate of the pairs, which become balanced. At this point the current neither grows nor decays and if another photon arrives, the diodes can't see it. In order to "shut down" this current the reverse bias voltage needs to be brought again below the breakdown voltage for a certain time. This process is called *quenching* and it can be accomplished by two types of circuits: *passive quenching* and *active quenching*. After sufficient time the reversed bias voltage is brought above the breakdown value, in order to turn on again the APD. With a fast active-quenching circuit the APD can be reset after a detection in few nanoseconds, and can be used as a photon-counting device in a PET camera, instead of a more classic photomultiplier tube [3]. A scheme of an avalanche photodiode and the presentation of the Geiger-mode process are shown in Figure 2.6.

There are some important aspects of the APD operated in Geiger mode, that need to be noted. The breakdown voltage is a function of the temperature. With lower temperature the noise decrease, and the breakdown voltage decreases as well. The avalanche process results in an intrinsic dark noise because a single photoelectron can be created thermally even in complete absence of light [26]. Taking into account

of the dark current of an APD is therefore important.

2.1.5 New PET camera design

In the last years there have been important improvements on PET imaging equipments, but progress are still far from having reached the best image quality possible for medical device and preclinical instruments. The most important instruments limitation in commercial PET are:

- non-uniform spatial resolution over the whole Field Of View (FOV) due to uncertainty on the Depth Of Interaction (DOI) in the scintillator,
- relatively low efficiency of photon conversion due to the correlation between the radial thickness of the scintillator and the DOI smearing of the radial coordinate,
- limited capability to recognize and reject Compton interactions in the crystals.

The most important goal is improving the spatial resolution (which is the capacity to discriminate two separate objects), the time resolution (which is the capacity to discriminate two different events in time) and the sensitivity (which is the capacity to efficiently detect the radiation emitted by the patient's body). Another important aim is the possibility to associate the PET to other morphological imaging like x-ray Computed Tomography (CT) or Magnetic Resonance Imaging (MRI)[14].
The standard geometry of PET is based on radial arrangement of the scintillator crystals, readout at one end by a photomultiplier tube. With this configuration, absent or limited DOI information causes parallax error, lowering the spatial resolution of the camera. Reducing the length of the crystals decreases this problem, but also compromises the sensitivity of the system. The axial concept avoids this compromise creating a configuration with resolution and sensitivity independent from each other [5].

The idea of using axially arranged long scintillator with readout on both of the sides started 25 years ago, but only recently developed. Recent works were based on 10 cm long LYSO crystal bars arranged in axial stack and readout on both sides with Hybrid Photon Detectors [4]. The different orientation of the detectors is shown in Figure 2.7. The axial coordinate was determined from the ratio of the light measured on both sides of the crystal. Another approach is proposed by AX-PET [5] with again an axial arrangement of long and individually read scintillating crystals aligned parallel to the axis of the scanner (Z-axis). The X-Y coordinates are given by the position of the hit crystal, with a resolution determined by the cross-section of the crystals. The third coordinate (Z) is given by many layers of wavelength shifting (WLS) plastic strips, which are placed, with a small air gap, below each crystal layer in the perpendicular direction. Both the crystals and the

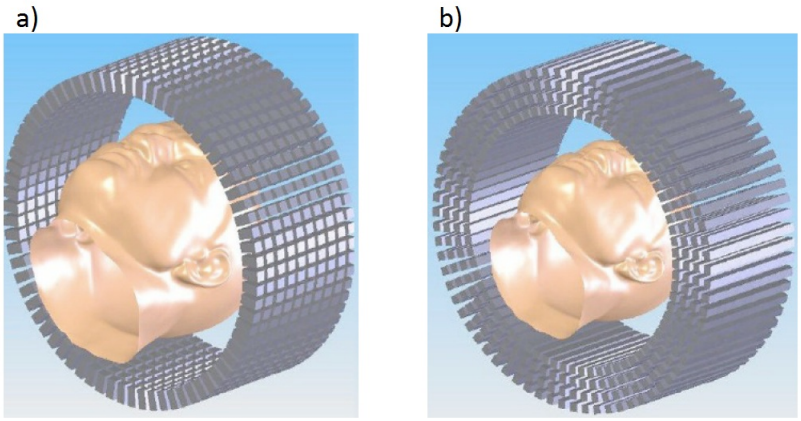

Figure 2.7: a)Radial orientation of the detectors inside a classical PET b) Axial orientation of the detectors for the new concept of PET [10].

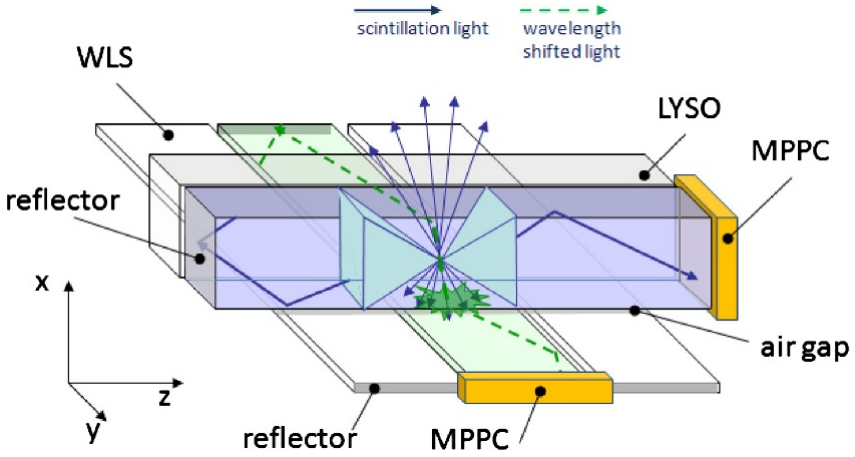

Figure 2.8: Principle of the light propagation and principle of the axial coordinate readout using scintillating crystals and WLS strips [5]

WLS are individually readout with an APD, in Geiger mode. The not read ends of the crystals and of the WLS are covered by a thin reflective Aluminum coating in order to send back the photons to the photodetector, as shown in Figure 2.8.

When a crystal is hit by a photon, it emits isotropically a correlated amount of scintillation light. Part of these photons are emitted within the angle of total reflection on the scintillator and travel to the end of the crystal bar, where they are read by the APD. The photons which are emitted outside the cone of total reflection, forward the crystal bar sideways and enter some wavelength shifter strips. The WLS material absorbs these photons and remits them shifting the wavelength. A fraction of these wavelength shifted photons can travel, by total reflection, till the end of the WLS, where can be read by another dedicated photodetector. The X and Y coordinates of each hit crystal are given by its position in the stack with digital resolution $\sigma_{x,y} = d/\sqrt{12}$ (where d is the transverse dimension of the crystal bar), the same applies for all WLS strips. In general more than one WLS strip has a detectable signal, the Z coordinate can be obtained either by using just the strip with the highest signal or using an analog interpolation using several strips,

thus improving the spatial resolution [4]. The very high optical transparency of the scintillating crystals is not good for the light sharing, but the new concept of reading scintillators via wavelength shifters, together with new small APD photodetectors, allowed to create this new axial readout for PET [5].
The biggest advantage of this new configuration is that sensitivity and spatial resolution are at a high degree uncorrelated. The number of layers in the direction of the incoming γ photons can be adjusted without affecting the spatial resolution, unlike in the conventional PET camera where the DOI uncertainty increases with the length of the crystals. In this way the spatial resolution becomes independent to the location where the annihilation occurs and the parallax error is avoided [4]. The Avantomography demonstrator described in this thesis is based on AX-PET idea and its main characteristics.

3. METHODS

In this chapter the geometry of the modules, the main properties of all of the components used to build this new axial PET demonstrator and the readout are described.

As mentioned before the Avantomography prototype originates from the AX-PET concept [5] and its main characteristics. The demonstrator consists of two adjustable parts placed in two different modules. Each Avantomography module consists of two layers of scintillator crystals in one part, two layers of scintillator crystals and two layers of WLS strips in the second part. Crystals and wave length shifter strips are readout by a novel type of G-APDs. The electronic chain consists of a 64 channels data acquisition system coupled to a 64 channels distribution system.

3.1 Scintillating crystal bars

The scintillating bars are LYSO crystals ($Lu_{1.8}Y_{0.2}$-SiO_5:Ce) produced by Saint-Gobain, marked as PreLude®420 [21]. This material is useful for PET applications thanks to its high density and the short decay time. The PreLude 420 is a lutetium-based scintillator which contains the radioactive isotope of ^{176}Lu, which is a β^- (electron) emitter. This isotope decays to the 597 keV excited state of ^{176}Hf for the 99.66% of the times. This state decays with a three gamma ray cascade of energies 307 keV, 202 keV and 88 keV. Nearly 100% of the β^- particles are absorbed inside the crystal (1" diameter by 1" long), but some of the photons can escape and can be detected from outside. One single crystal of 1" diameter by 1" long has then a set of beta+gamma distribution shown in Figure 3.1 b) . The intrinsic activity is 39 cps/g [21].
The wavelength of the emitted scintillation light matches well with the sensitivity spectrum of most of photodetectors, particularly the detectors used for this thesis that will be described in Section 3.3. The emission curve and the beta distributions of the LYSO are shown in Figure 3.1 and its properties are shown in Table 3.1.

The LYSO crystals used in this demonstrator are 150 mm long with a cross section of 3×3 mm^2. All surfaces are optically polished, the edge are sharp and crack-free. The crystals are not wrapped or coated, except for the non-read out face opposite to the photodetector, which is coated with white teflon tape (PTFE).The edge attached to the photodetector is also coated with the teflon tape on the long sides for about 10 mm. The white teflon tape is a good diffused light reflector, this

Table 3.1: Properties of the LYSO crystal used in Avantomography demonstrator [21].

Property	
Density (g/cm^3)	7.1
Hygroscopic?	No
Attenuation length for 511keV (cm)	2.88
Wavelength of emission max λ (nm)	420
Index of refraction at emission max	1.81
Decay time (ns)	41
Light output (photons/keV)	32

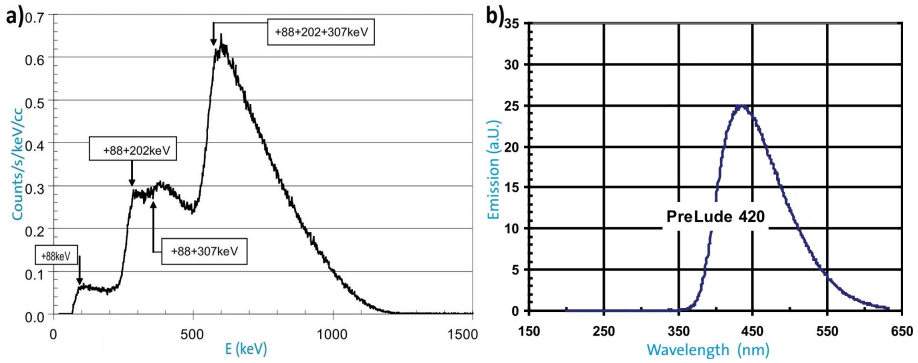

Figure 3.1: a) Beta distributions of a single crystal (1" diameter by 1" long) of PreLude^{TM} 420 b) Emission spectrum of PreLude^{TM} 420 [21].

coating technique can thereby improve the performance of scintillator readout with the photodetectors.

3.2 Wavelength Shifting strips

The wavelength shifting (WLS) strips are made in EJ-260-10 from Eljen Technology [11]. This material is based on Polyvinyltouluene (PVL) with a very high dye concentration and a wavelength of emission maximum at 490 nm. The material is a green emitting plastic scintillator suitable for use when longer wavelengths are required and for optical coupling to solid state photosensors. The wavelength of the emitted light matches well with the sensitivity spectrum of the photodetectors used for this prototype [11]. The emission spectrum of the WLS is shown in Figure 3.2 and its properties are shown in Table 3.2.

The WLS strips used in this demonstrator are 15 mm long with a cross section of $3 \times 1\text{mm}^2$. All surfaces are optically polished, the edge are sharp and crack-free. The strips are not wrapped or coated, except for the non-read out face opposite to the photodetector, which is coated with a reflective non metallic ultra-high reflective film Vikuiti^{TM} Enhanced Spectacular Reflector (ESR) from 3M. The ESR is a non-metallic mirror-like optical enhancement film based on multi-layer polymer technology, its reflectance is $> 98\%$ and the thickness is 65 μm [2]. Around the read out edge of the strips a dark double-sided tape was placed in order to isolate each strip from the light emitted by the neighbouring ones and to keep the photodetector

Table 3.2: Properties of the WLS strips used in Avantomography demonstrator [11].

Physical and Scintillation Constants	
Light output % Anthracene	60
Scintillation efficiency (photons/1MeVe^-)	9200
Wavelength of emission max λ (nm)	490
Decay time (ns)	9.2
No. of H atoms per $cm_3 \times 10^{22}$	5.21
No. of C atoms per $cm_3 \times 10^{22}$	4.70
No. of electrons per $cm_3 \times 10^{23}$	3.35
Density (g/cm_3)	1.02
Polymer Base	Polyvinyltoluene
Refractive Index	1.58

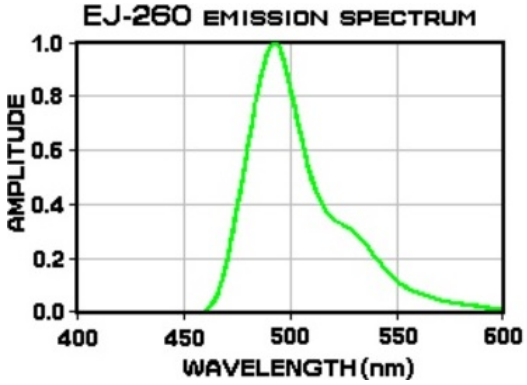

Figure 3.2: The WLS emission spectrum [11].

in its correct position.

3.3 Photodetectors

The LYSO crystals and the WLS strips are individually read out by fast Geiger-mode Avalanche Photo Diodes from Hamamatsu, marked as MPPC® S10931-050P [13]. The MPPC is a new type of opto-semiconductor device that offers the high performance needed in photon counting and can be used in different application for detecting weak light at the photon-counting level, as in PET. It also has the good advantage of a low bias voltage. The electrical and optical characteristics of the MPPC are shown in Table 3.3. The photon detection efficiency of the MPPC is shown in Figure 3.3. The wavelength of the maximum of this curve is around the wavelength of the peak of the scintillating light emitted by crystals used in this thesis, shown in Figure 3.1.

The MPPC used for this demonstrator have an effective active area of 3×3 mm^2, subdivided in 3600 pixels of size 50×50 μm^2. The MPPCs are biased in parallel, each module of the device is biased independently. The bias voltage is provided by the commercial unit IQSP582 from Vertilon, which also collects the output signals

[1] Ratio of the active area of a pixel to the entire area of the pixel
[2] 0.5 p.e (threshold level)
[3] 0.5 p.e (threshold level)
[4] Single photon level

Table 3.3: Properties of the MPPC used in Avantomography demonstrator [13].

Electrical and optical properties	
Fill factor (%) [1]	61.5
Spectral response range λ (nm)	320 to 900
Peak sensitivity wavelength λ_p (nm)	440
Operating voltage range (V)	70 $\pm$ 10
Dark count (Mpcs) [2]	6
Dark count Max. (Mpcs) [3]	10
Terminal capacitance Ct (pF)	320
Time resolution (FWHM) (ps) [4]	500 to 600
Temperature coefficient of reverse bias (mV/ ℃)	56
Gain	7.5×10^5

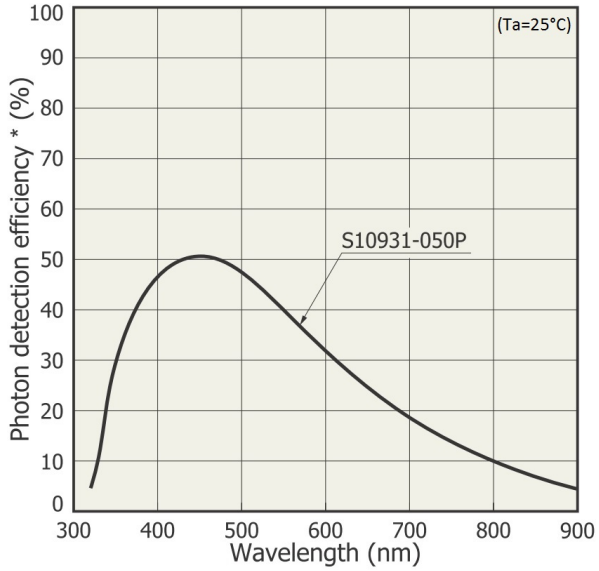

Figure 3.3: The MPPC detection efficiency as a function of the wavelength of the incident light (at 25℃) [13]. *Photon detection efficiency includes effects of crosstalk and after pulses.

from the photodetectors. This unit has many functions controlled by a LabView [18] program and will be described in Section 3.4.

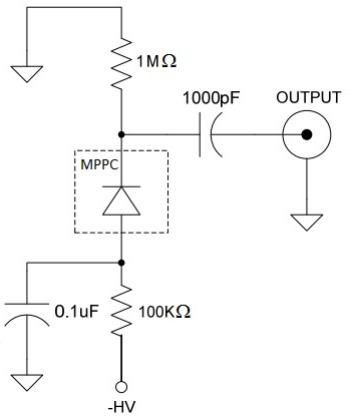

Figure 3.4: The circuit for biasing the MPPCs.

The bias circuit for the MPPCs is shown in Figure 3.4. The 1 MΩ resistor

maintains a zero voltage at the cathode of the MPPC when the coupling capacitor is used. The 1000 pF capacitor blocks some of the dark current. The 0.1 μF and the 100 kΩ form the bias filter network. The -HV is the negative high voltage supply from the bias supply on the IQSP582 unit. The MPPC boards are connected in parallel in order to share the bias supply. The OUTPUT goes to the SDS232 front panel, connected to the IQSP582 unit, that collects and processes the signal. This function will be described in Section 3.4.
The gain value is chosen to optimize the photon detection efficiency (PDE), keeping the dark noise and optical cross-talk at an acceptable level. Because of the relatively short measurement time, no temperature correction is applied for the MPPC gain in this set-up.

3.4 Readout Electronics and data acquisition

The Avantomography demonstrator provides analogue readout electronics for all the crystals and all the WLS strips. Each MPPC is connected via a thin cable to each individual bias circuit (described in the previous section). The bias circuits are connected in parallel inside electronic boards in groups of 8. Each module of the demonstrator has 4 boards connected in parallel and is individually biased.
The electronic chain is based on the PhotoniQ IQSP582 64 Data Acquisition System from Vertilon [24]. The PhotoniQ is an all-in-one laboratory instrument suitable for PET application providing different features. It is used for the biasing of the MPPCs, but also for the charge integration and the data acquisition. It is a precise and high speed 64 channels parallel system, capable of providing real-time digital signal processor (DSP) based signal, processing input events and sending the digitized signals to a computer, through a PC interface. The PhotoniQ provides intelligent triggering modes: edge, internal, level, input, pre-trigger and cross bank.

- Edge trigger is a simple trigger mode where an externally-supplied positive signal edge starts the event acquisition process.
- In internal triggering mode the unit operates a continuous data acquisition. A programmable internal free running clock replaces the external trigger signal. Data is continuously acquired on each edge of the clock signal. This mode is particularly useful when large blocks of event data are needed for collection and analysis, but no trigger signal is available.
- Level trigger mode is similar to internal triggering except that an externally provided positive level-sensitive trigger gate controls the acquisition of events. The actual trigger signal is internally generated but it is synchronized and gated by the external trigger gate.
- Input mode is used to trigger the acquisition process when incoming data on a specific channel exceeds a defined threshold. No external trigger signal is

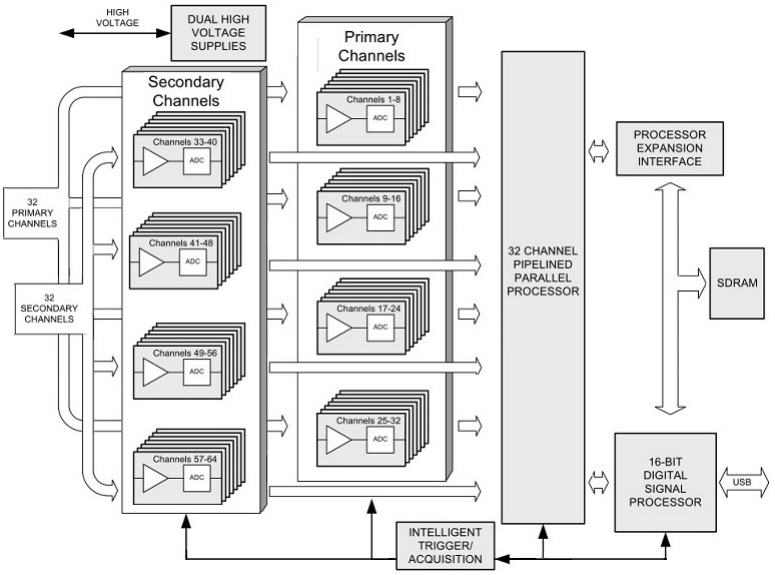

Figure 3.5: 64 channels functional block scheme of the acquisition module, implemented in the IQSP582 Data Acquisition System [23].

required. The charge integrated during the integration time is compared to the trigger threshold level, if its value crosses the threshold the PhotoniQ acquires data across all the channels.

- In pre-trigger mode, an external positive edge sensitive trigger signal is used to acquire event data that occurred prior to the arrival of the trigger.

- In cross bank mode one or more channel banks can be triggered with one set of parameters which in turn trigger other banks using a different set of parameters. In a typical example, a bank is set up as an input trigger type with a particular integration period. The other banks are set up with different delays and integration periods. When an input event crosses the specified threshold on the first bank, the other banks can then be triggered. Data acquisition on these banks occurs with their respective specified delays and integration periods.

The 64 channel model is made up from four independently configured and triggered banks of 16 channels. Each bank generates eight parallel signals of digital data. The intelligent module configures the triggering and acquisition parameters for each bank. The digital data channels are output to the Pipelined Parallel Processor (P3) which performs data channel offset and uniformity correction. The resulting data is sent to the DSP where it is packed and sent to the USB output port. Additional reserved DSP processing power can be used to implement user defined filter, trigger, and data discrimination functions [23]. The scheme of the functionality of the multi-channel data acquisition system is shown in figure 3.5.

Data acquisition starts when a trigger signal is detected by the PhotoniQ intelligent trigger module. The collection and the following digitization of charge signals

Table 3.4: Specifications of the PhotoniQ 64 channel data acquisition system used in the Avantomography demonstrator [24].

Specifications	
Number of channels	64
Resolution (bits)	14
Dynamic Range (dB)	84
Equivalent Input Noise Charge (fC RMS typ.)	100
Maximum Imput Signal (pC)	877
Channel-to-Channel crosstalk typical (dB)	-84
Channel-to-Channel crosstalk max (dB)	-80
Input Bias Current typical (pA)	±40
Input Bias Current max (pA)	±150
Maximum Trigger Rate (MTR) (kHz)	250
64 Channel Sustained Average Event Rate (SAER) (event/s)	35 000
8 Channel Sustained Average Event Rate (SAER) (event/s)	240 000
Power Consumption typical (W)	4.5
Power Consumption max (W)	5.5

Table 3.5: Specifications of a single 32 channels SMB distribution system [25].

Specifications	
Number of channels	32
Input Noise Charge (fC)	55
Maximum Charge Signal (pC)	500
Crosstalk (dB)	<84
Panel Connector Type	SMB Male Bulkhead Jack

from the photodiode sensors are simultaneously made across all the channels. This functionality, shown in the figure 3.5 as an amplifier followed by an analog-to-digital converter (ADC), is implemented as precision analogue circuit elements that integrate, amplify, and digitize the charge. The parallel architecture of this circuit allows charge integration and digitization to take place simultaneously across all channels. This design permits the acquisition of very narrow charge pulses with single photon sensitivity at very high rates and allows also the achievement of very high data acquisition speeds. The PhotoniQ is programmed by the Control and Acquisition Interface System, a software with graphical user interface, that allows to configure and monitor the operation of the unit (data acquisition, trigger mode, integration time, processing functions, etc.) [23]. The specifications of the 64 channels data acquisition system are shown in Table 3.4.

The multiple single photodetectors are interfaced to the multichannel and data acquisition system through two SDS232 channel SMB (Server Message Block) distribution systems, from Vertilon [25]. One module provides electrical connectivity between the PhotoniQ multi-channel and data acquisition system, up to 32 charge output devices. Each MPPC is connected to a single channel of the front panel of the distribution boards through a coaxial cable. The SDS232s are connected on their back panel to the PhotoniQ through a low-noise connector. The specifications of the channel distribution system are shown in Table 3.5.

The sketch of the configuration of the electronic chain is shown in Figure 3.6. The figure shows one MPPC attached to one LYSO crystal, one MPPC attached to one WLS strip, the bias board, the Vertilon apparatus and a PC with the PhotoniQ software.

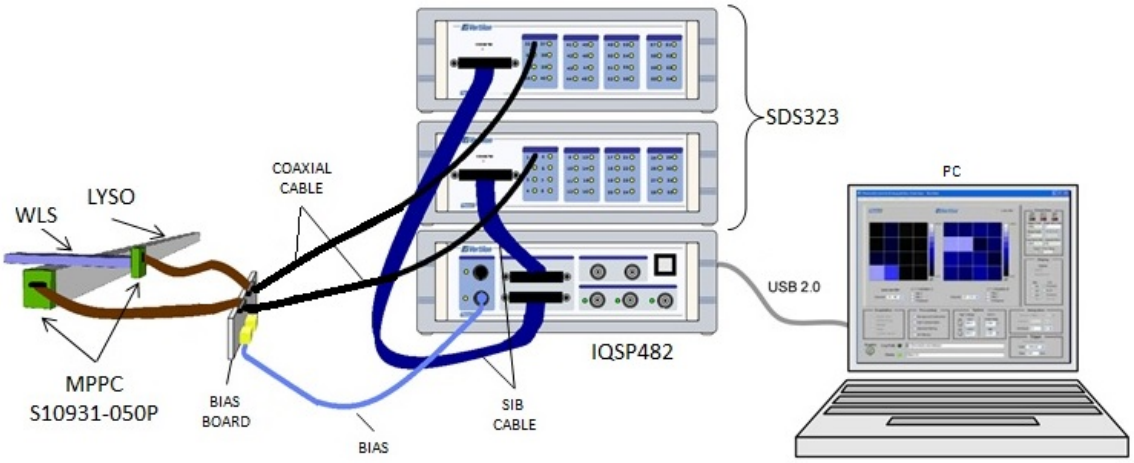

Figure 3.6: Sketch of the configuration of the electronic chain.

3.5 Mechanical Assembly

The mechanical design of the Avantomography demonstrator requires different conflicting arrangements, like compactness, positioning precision, best optical assembling, portability and robustness. The demonstrator consists of two identical parts which contain two modules each. One module contains two layers of scintillator crystals, the second module has two layers of scintillator crystals and two layers of WLS strips in it. Each first layer has three LYSO crystal bars and the second two bars, each layer of WLS has 11 strips, for a total of 20 LYSO crystals and 44 WLS strips. The LYSO bars are placed in the trans-axial plane with the WLS placed orthogonally. Scintillators and wave length shifter strips are readout by a single MPPC, the electronic chain consists in the commercial 64 channels data acquisition system coupled to the 64 channels distribution system, as described in the previous sections.

In order to create a small and light device the highest possible packing density is reached, in accordance with the dimensions of the photodetectors. The crystals are placed inside containers made with non conductive and non transparent material in order to hold them in place with minimal mechanical contacts and shield them from external light. The two crystals of the upper layer are staggered from the other layer along the Y direction by half the crystal pitch (1.75 mm). A layer of 11 WLS strips is mounted above each crystals layer with an air gap of 0.2 mm. The 11 WLS of each layer are placed along Y direction in the center of the length of the crystals. The two layers are optically separated by a thin sheet of the same non conductive

and non transparent material. The structure of a single module is shown in Figure 3.7.

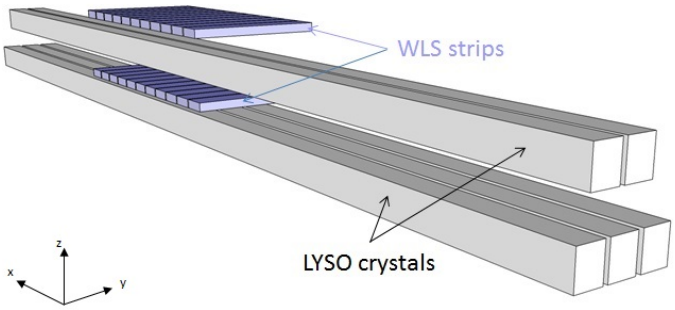

Figure 3.7: Assembling of the crystals and the WLS inside one Avantomography module.

The MPPCs are attached to the bias circuit with a silver-filled epoxy EPO-TEK®EE129-4 from Epoxy Technology. This room temperature cure, silver-filled epoxy is designed for making electrical connections in circuit assembly, semiconductor, and LCD applications [12]. Because of the larger surface of the active area of the MPPC (3×3 mm^2) compared to the section of the WLS strips (3×1 mm^2), a thick dark double-sided tape is used to keep the MPPC in place and cover the unused active area. The MPPCs are attached to the LYSO crystal bars and the WLS strips with an optically clear adhesive 8172CL by 3M, with light transmission $\sim 99\%$[1]. A thin foil of dark plastic is placed between two adjacent MPPC in order to avoid electrical conduction and propagation of light between them. With this configuration the structure can be easily disassembled in view of possible repairs, replacements or further innovations. The entire module structure is contained inside a light plastic box that creates the L shape of each module. A picture of the two modules of the Avantomography demonstrator is shown in Figure 3.8.

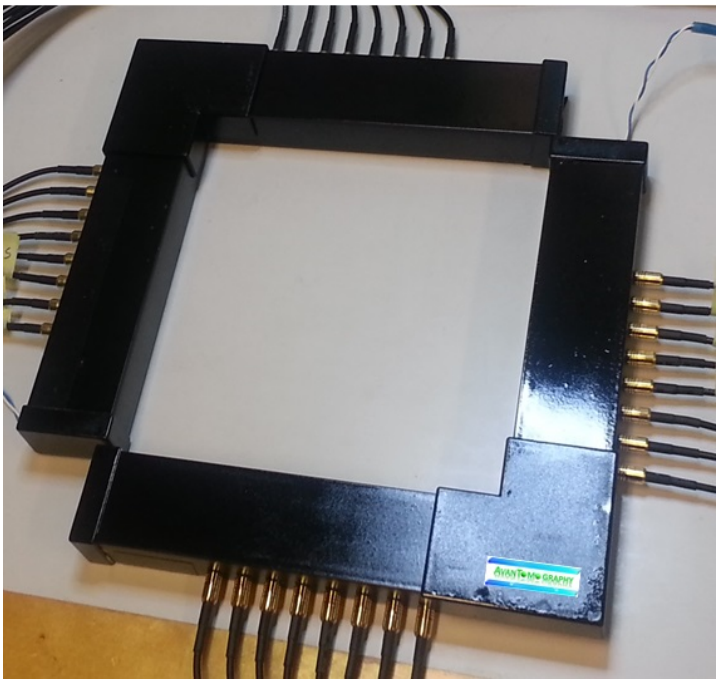

Figure 3.8: The Avantomography demonstrator.

4. EXPERIMENTAL SET-UP AND MEASUREMENTS

The final aim of this thesis is the construction and the energy calibration of the demonstrator. For this reason after the modules are assembled, the intrinsic radioactivity of the LYSO crystals and the photoelectric peak at 511 keV of a positron emitter sources are measured. In this chapter the experimental set-up built for the acquisition of these measurements is described.

4.1 Intrinsic radioactivity of LYSO

As illustrated in Section 3.1 the LYSO crystals used in this device contain the radioactive isotope ^{176}Lu, which is a β^- emitter. This isotope decays for the 99.66% of the times to the 597 keV excited state of ^{176}Hf, which relaxes with a 3 gamma ray cascade of energies 307 keV, 202 keV and 88 keV. The β particles lose all their energy inside the same crystal where they are produced and can't be detected from outside. The probability of internal absorption of the photons emitted for intrinsic radioactivity inside the crystal itself is instead very low. For this reason the typical energy distribution of intrinsic radioactivity of one single crystal placed inside a matrix of LYSO bars is mostly given by the photons emitted from the nearby crystals. The intrinsic activity of LYSO is 39 cps/g. In the Avantomography demonstrator the crystals are 20, with $3\times3\times150$ mm^3 dimensions and a density of 7.1 g/cm^3. It implies an activity of about 374 Bq of β^- decays out of a single crystal, corresponding to a total activity of $\sim$ 7.5 kBq ($\sim$ 7.5 kHz of rate) for all the crystals. During the acquisition the trigger is set in internal mode, in this way the device continuously collects the integrated charge signals from the photodetectors and the data is acquired simultaneously across all 20 channels (only the channels connected to the LYSO crystals are acquired). Ideally the integration time should match the scintillation time of the LYSO. The drawback to this is that the entire system has some dead time (MPPC quenching time, electronic delay etc.), if the integration time matches the scintillation time there is a very strong possibility that the timing does not align and therefore a fraction of the charge from the scintillation event is not acquired. Since the natural activity of the LYSO is low and then the events are infrequent, the integration time is increased to the point where the device has an acceptably probability of acquiring a scintillation event. Moreover if the integration time is too long then two separate events might be captured together and incorrectly recorded as a single one.
The decay rate on a single channel is therefore considered, since all channels in the

system operate simultaneously and independently. So at 374 Bq the average time between events is about 2.7 ms. Based on Poisson statistics, if making the integration time a factor of 100 lower, then the likelihood of acquiring two events and interpreting them as one is quite low, therefore 27 μs is estimated as upper bound for the integration time. For the lower bound the probability of "splitting" a scintillation event is approximated as equal to the ratio of the scintillation time of the LYSO ($\sim$ 100 ns) divided by the integration time:

$$Probability\,of\,splitting\,two\,events = \frac{scintillation\,time}{minimum\,integration\,time}. \tag{4.1}$$

Considering a probability of 1% the integration time is then:

$$Minimum\,integration\,time = \frac{scintillation\,time}{probability\,of\,splitting} = \frac{100\,\text{ns}}{0.01} = 10\,\mu\text{s}. \tag{4.2}$$

Given this, the intrinsic radioactivity of the LYSO crystal is measured with the settings presented in Table 4.1. The set-up of the experiment for the acquisition of the intrinsic radioactivity of the LYSO is shown in Figure 4.1. The 4 modules are placed all together in order to create one single block of 20 crystals, in this way the number of photons produced that can hit one single bar is higher. The measurement is therefore acquired from the central crystal, because it has the probability to absorb the highest number of photons. The run is performed without any radioactive

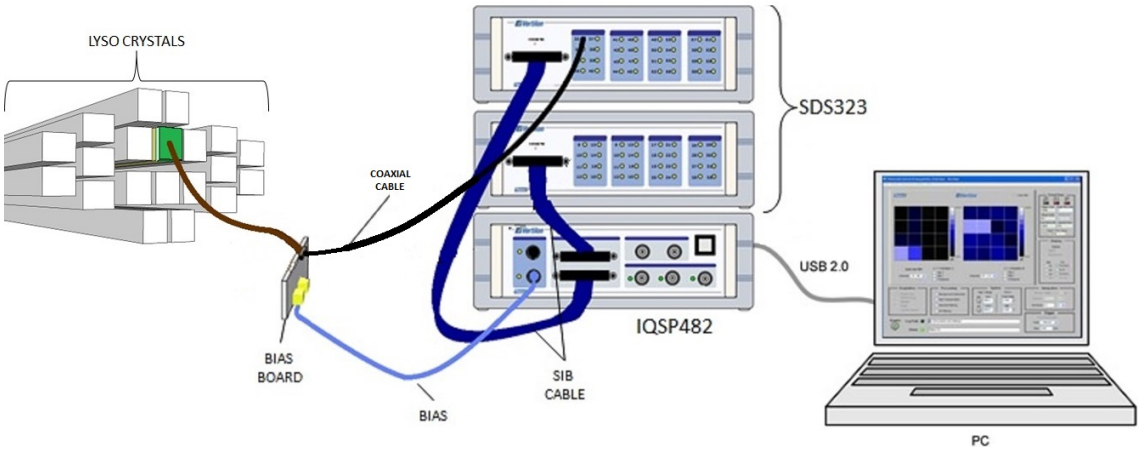

Figure 4.1: Set-up for the measurement of the intrinsic radioactivity of the LYSO. The 20 LYSO bars are placed all together forming one bloc inside a dark-room box. The selected crystal is the only one connected to the acquisition system in the sketch.

source, with the crystals placed in a dark-room box, for three hours. The intrinsic radioactivity spectrum, obtained from the data acquired with this measurement, is shown in Figure 4.2.

The data analysis and the results will be described in details in the following chapter.

Table 4.1: Settings applied to the demonstrator for the acquisition of the LYSO intrinsic radioactivity.

Settings for measurement of the intrinsic radioactivity	
Number of channels	20
Trigger Mode	Internal
Integration Time (μs)	10
Internal Trigger Rate (Hz)	200k
Bias Voltage (V)	74
Total time of acquisition (hours)	3

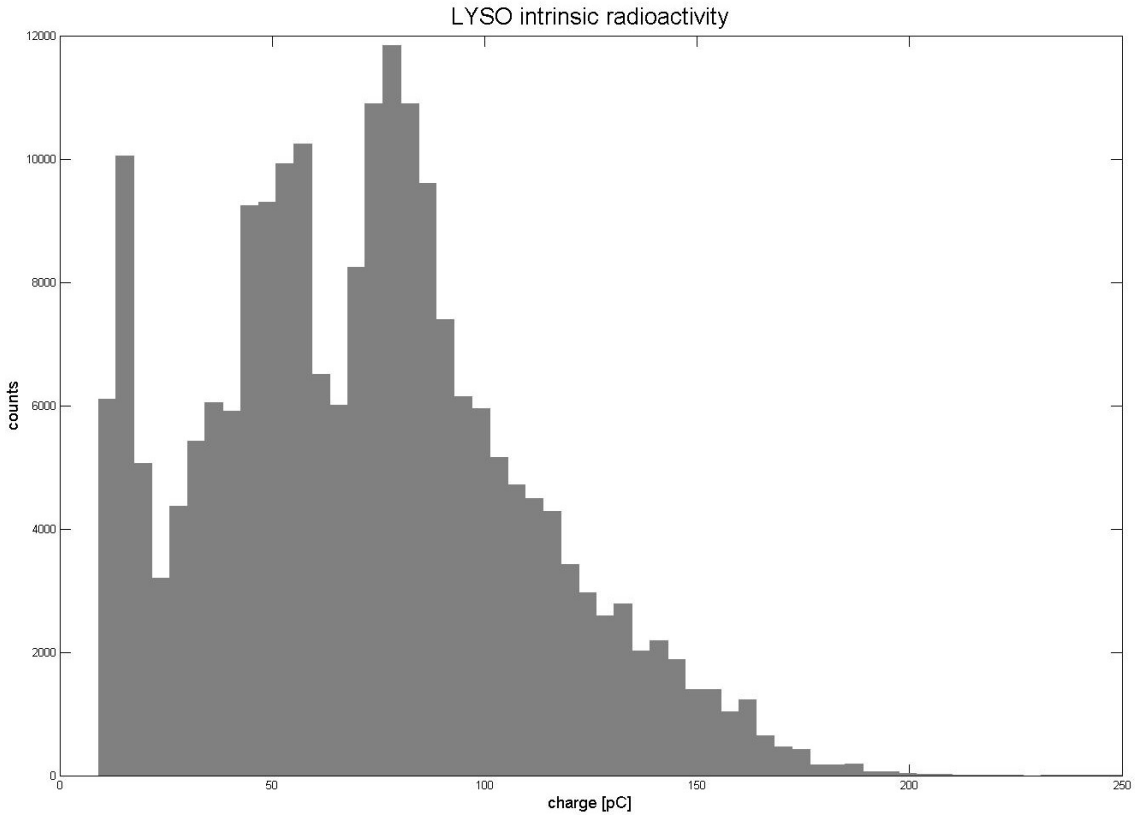

Figure 4.2: Charge spectrum of the intrinsic radioactivity of one LYSO crystal.

4.2 Photoelectric peak of 511 keV photons

For the characterization of the basic properties of each single module, photoelectric absorption events are measured. The measurement performed at the Tampere University Hospital allows to test the demonstrator simulating a PET basic test. The experimental set-up has been built with a photon emitter source of known energy and controlled activity over the surface of the device. The ^{68}Ge/^{68}Ga radioactive source, used to perform the measurement is a standard linear source, normally used for PET calibration. The ^{68}Ge is used as a parent isotope of the ^{68}Ga. The halflife of the ^{68}Ge is 271 days, it decays only with electron capture in ^{68}Ga, which is the real positron emitter (with a half-life of 68 min). The active part of the source is 160 mm long, with an inner diameter of 1 mm, an external diameter of 1.5 mm and a linear density of activity of 0.4 MBq/cm. The source is placed in the center of the Field

Of View (FOV) of the demonstrator, in order to equally irradiate all the modules. The set-up of the experiment for the acquisition of the 511 keV photoelectric peak is shown in Figure 4.3 and the sketch of the positioning of the rod source in the center of the FOV is shown in Figure 4.4.

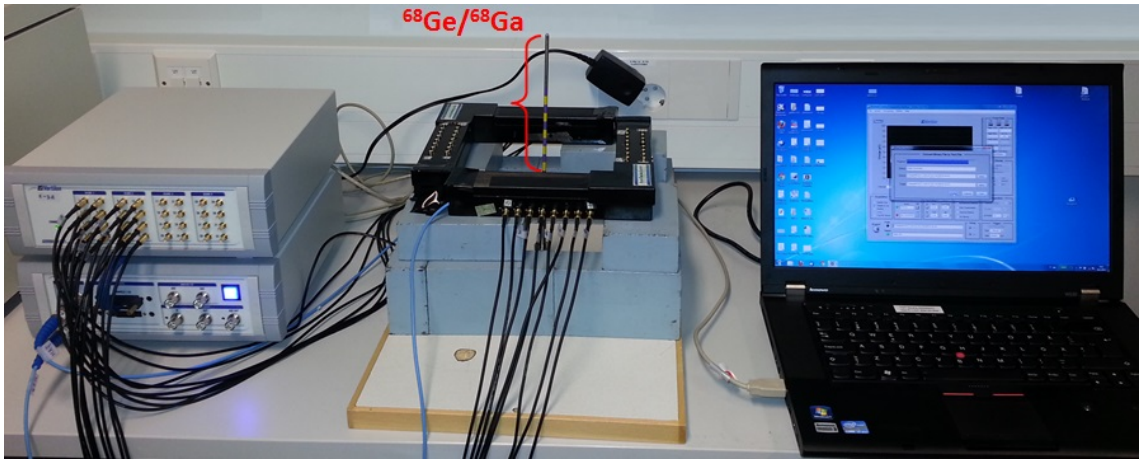

Figure 4.3: Set-up for the measurement of 511 keV photoelectric peak of a ^{68}Ge/^{68}Ga radioactive source. The source is placed in the center of the (FOV) of the device as visible in the picture.

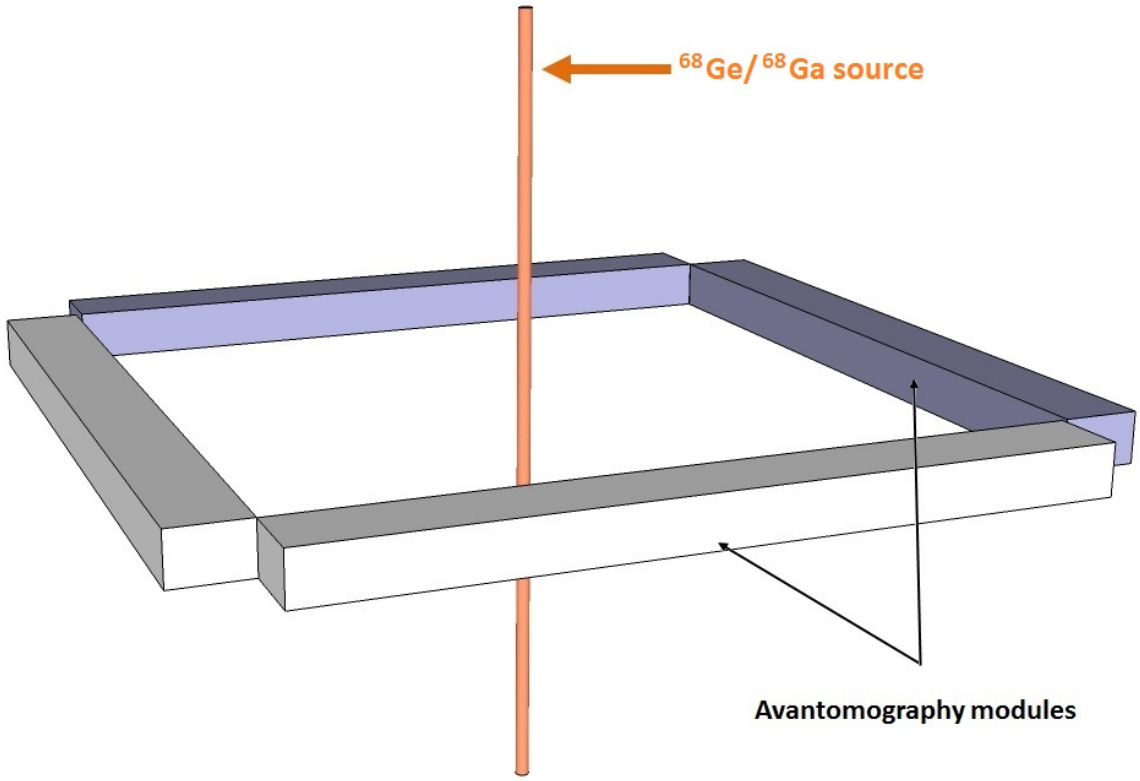

Figure 4.4: Sketch of the experimental set-up. The source is placed in the center of the (FOV). The radioactive part goes 8 cm below the center and 8 cm above, irradiating equally the 4 modules.

Considering the distance between the source and the device (10.6 cm) the flux of photons that impacts to it, is about 5 kBq/cm^2. Considering also that with two layers of crystals, only 40% of the photons can be detected [21]. The total flux is

Table 4.2: Settings applied for the acquisition of the charge spectrum of 511 keV photons.

Settings for the 511 keV photoelectric peak	
Number of channels	20
Trigger Mode	Internal
Integration Time (μs)	10
Internal Trigger Rate (Hz)	200k
Bias Voltage (V)	74
Total time of acquisition (hours)	3

then $\sim$ 2 kBq/cm^2, divided across 20 channels. Assuming that all the channels have an equal probability of detecting an event, the average activity rate is then 0.25 kBq per channel. The same calculation applied for the intrinsic radioactivity of the LYSO is used for the integration time for the measure with the ^{68}Ge/^{68}Ga source. At $\sim$0.25 kBq the average time between events is thus about 4 ms. Considering again the integration time a factor of 100 lower, 40 μs is set as upper bound for the integration time. The lower bound is again considered given by the scintillation time of the LYSOs and is 10 μs, as before. The run is then performed for three hours, with the settings presented in Table 4.2. The charge spectra of 511 keV photons detected in one LYSO crystal are obtained from the data acquired with this measurement. An example is shown in Figure 4.5, with spectrum acquired by the channel number 1.

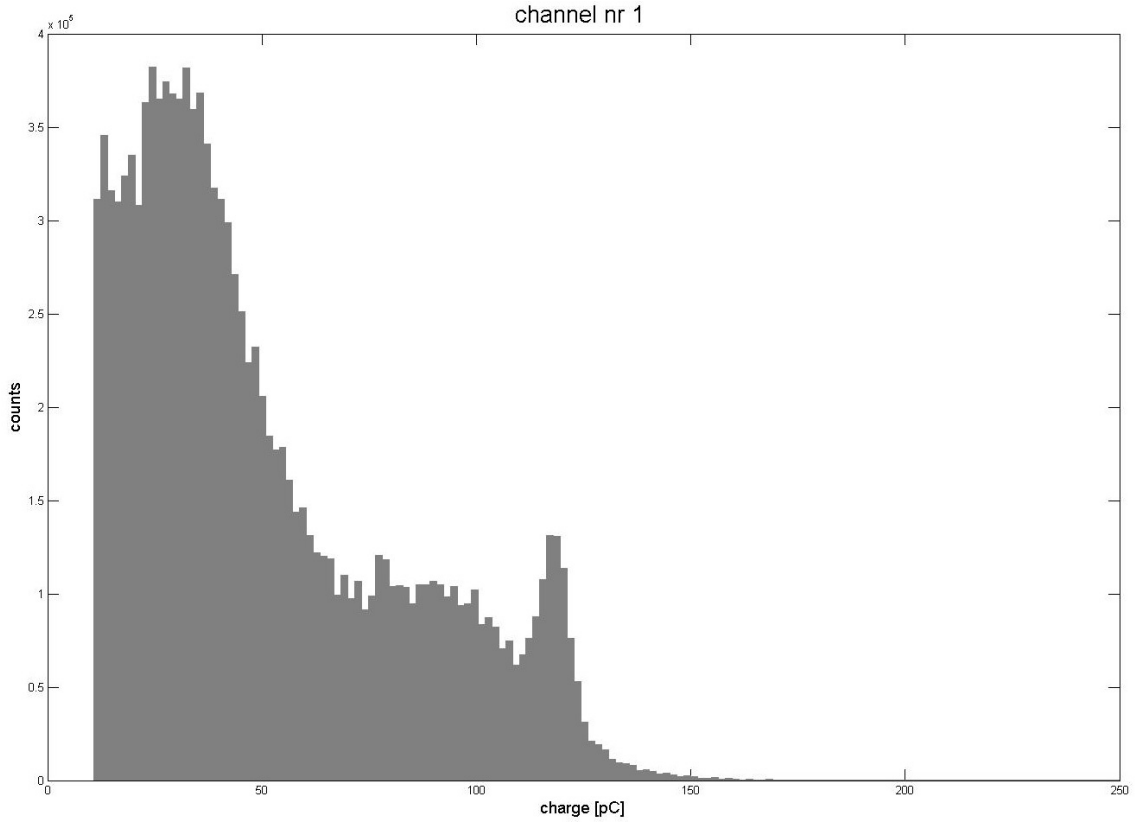

Figure 4.5: Charge histogram of 511 keV photons detected in LYSO crystal channel 1.

The data analysis and the results will be described in details in the following chapter.

5. DATA ANALYSIS AND RESULTS

In this chapter the data analysis applied on the acquired data and the results are shown.
A MATLAB based analysis code is applied on the data set. For each acquisition the PhotoniQ provides a data file (in its specific format), that can be converted in text file by the software itself. With the MATLAB code the raw data set can be read and analysed in order to extract all the relevant information (for example the energy of the interactions, and the time of the event). The data analysis is restricted to photoelectric absorption events, on the data different selection cuts are applied and different histogram are plotted. Using again a MATLAB based code, the energy calibration for the LYSO is extracted from the histograms and furthermore the energy resolution is calculated.

5.1 Intrinsic radioactivity of LYSO

The intrinsic radioactivity of one LYSO crystal is measured and analysed, the spectrum obtained with the data analysis is shown in Figure 5.1. A threshold of 10 pC is applied to the data, in order to eliminate the background signal given by dark current noise and low energy photons. An upper limit of 250 pC is applied as maximum. This range has been divided in 70 intervals of constant dimension and the histogram has been plotted. The spectrum is an histogram of the values of the charge collected during an acquisition of three hours. The continuous distribution in the spectrum represents the intrinsic radioactivity of one crystal bar, given by the β particles and the gamma photons that cannot escape from the crystal itself. The peaks are given by the γ produced within the crystals surrounding the considered channel. These photons, after they are produced, can escape and be absorbed by the selected crystal. The two highest peaks correspond to the typical de-excitation of the ^{176}Hf produced during the decay (202 keV and 307 keV) and are the typical lines for the intrinsic radioactivity of the LYSO. The lowest de-excitation photon (88 keV) cannot be detected, because of its high internal conversion probability. The third peak in the spectrum is given by the characteristic x-ray emission from the K-shell of the lutetium, that follows the photoelectric absorption of the photons, and corresponds to an energy of 55 keV [5].
A Gaussian fit is applied to each of the peaks in order to calculate the position and the standard deviation of them. The characteristics of the Gaussian fitting curves are calculated using a MATLAB dedicate code, that can evaluate all the parameters

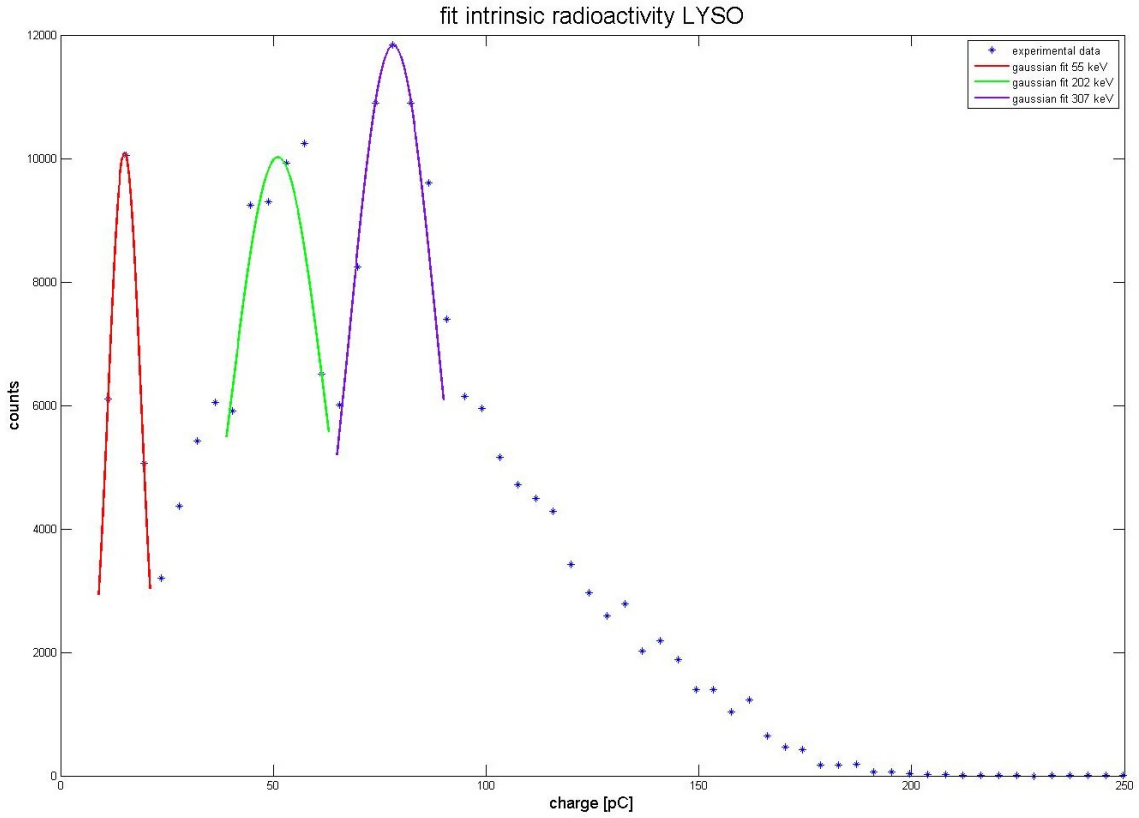

Figure 5.1: Charge spectrum of the intrinsic radioactivity of one LYSO crystal, with a Gaussian fit for each peak.

that define them:

$$f(Q) = \alpha * exp\left(-\frac{Q-\beta}{\delta}\right)^2 \tag{5.1}$$

The parameter α is the height of the peak of the curve, β is the position of the centre of the peak, and δ is the standard deviation. The coefficient of correlation between the fitting curve and the data is R^2. In this case the independent variable Q is the charge emitted by the photodetectors. Each group of 3 parameters is calculated for each fitting curve. The obtained values are shown in Table 5.1. The position of the peaks derives from the parameter β of each curve. In Table 5.2 the peak position

Table 5.1: Parameters of the Gaussian fit curves. The parameter α is the height of the peak of the curve, β is the position of the centre of the peak, δ is the standard deviation, and R^2 is the correlation coefficient.

Parameters of the Gaussian fit curves				
	α height of the peak [counts]	β mean value [pC]	δ standard deviation [pC]	R^2 correlation coefficient
gaussian fit 1	1.009e+004	15.04	5.439	1
gaussian fit 2	1.002e+004	51.80	15.58	0.833
gaussian fit 3	1.183e+004	78.16	14.52	0.9752

Table 5.2: Peak position and relative energy.

Curve	pC	keV
gaussian fit 1	15.04	55
gaussian fit 2	51.08	202
gaussian fit 3	78.16	307

in pC and the correspond energy in keV are listed for each curve. The positions of the peaks of the intrinsic radioactivity of the LYSO crystal are used for the energy calibration, as explained in section 5.3.

5.2 Photoelectric peak of 511 keV photons

The spectrum of 511 keV photons absorbed by one LYSO bar is measured and analysed. It is shown in Figure 5.2, with a Gaussian fit on the photoelectric peak. A threshold of 10 pC is applied to the data, in order to eliminate the background noise and low energy photons. An upper limit of 250 pC is applied as maximum. This range has been divided in 150 intervals of constant dimension and the histogram has been plotted. The spectrum is an histogram of the values of the charge collected during the acquisition with the ^{68}Ge/^{68}Ga source placed in the center of the FOV. This graph represents the typical energy distribution of all of the events occurred inside the LYSO crystal during the three hours long acquisition. The continuous on the left side of the photoelectric peak is due to all the other events that occurs together with the photoelectric absorption. These events are mostly given by:

- background radiation and cosmic rays;
- K_α and K_β x-ray photons emitted for the de-excitation that follows the electronic capture;
- Compton effect;
- effects due to the surrounding materials (characteristic x-rays, backscattering, diffused photons, etc.);

All these events degrade the spectrum, creating the continuous noise at low energies, visible in the plot. A Gaussian fit is applied to the photoelectric peaks in order to calculate its position and its standard deviation. The characteristics of the Gaussian curve are again obtained using the MATLAB dedicate code, that calculate all the parameters:

$$f(Q) = \alpha' * \exp\left(-\frac{Q-\beta'}{\delta'}\right)^2 \tag{5.2}$$

Where the independent variable Q is, again, the charge emitted by the photodetectors. The parameter α' is the height of the peak of the curve, β' is the position of the centre of the peak, and δ' is the standard deviation. The coefficient of correlation

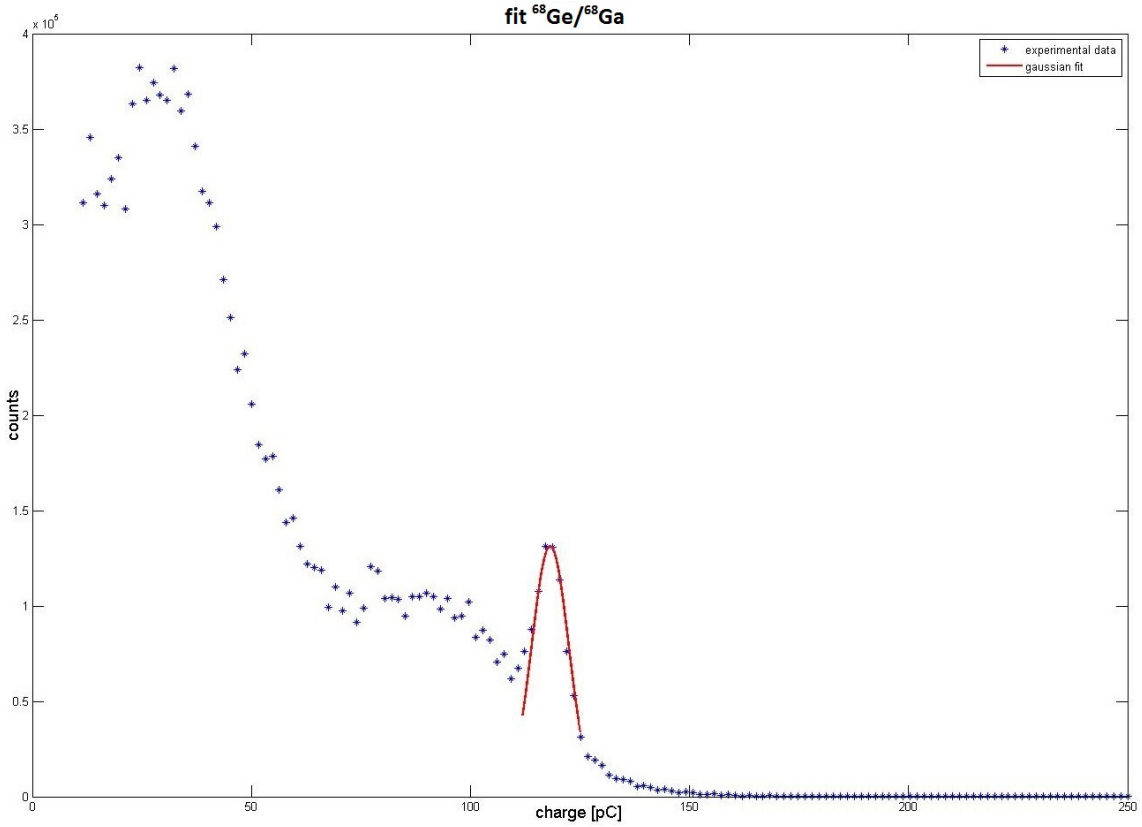

Figure 5.2: Charge spectrum of the 511 keV photons detected in one LYSO crystal, with a Gaussian fit for the photoelectric peak.

Table 5.3: Parameters of the Gaussian fit curve for the photoelectric peak. The parameter α' is the height of the peak of the curve, β' is the position of the centre of the peak, δ' is the standard deviation and R^2 is the coefficient of correlation between the fitting curve and the data.

Parameters of the Gaussian fit curve				
	α' [counts]	β' [pC]	δ' [pC]	R^2
gaussian fit	1.313e+005	118.2	5.856	0.9833

between the fitting curve and the data is R^2 The parameters obtained are shown in Table 5.3. The position of the peak derives from the parameter β' of the curve. In Table 5.4 the peak position in pC and the correspond energy in keV are displayed. This value is used for the energy calibration, together with the intrinsic radioactivity of the LYSO, as explained in section 5.3.

5.3 Energy calibration

The measure of the intrinsic radioactivity of the LYSO and the 511 keV photoelectric peak are used for the energy calibration of the crystals of the Avantomography demonstrator. The energy calibration consists in the conversion from the charge units (pC) to the energy scale (keV). This procedure has two purposes, the equalization of all the channels and the correction of the MPPCs response, which is not

Table 5.4: Peak position and relative energy.

Curve	pC	keV
gaussian fit	118.2	511

Table 5.5: Peak position, relative energy and relative error (standard deviation) of the LYSO intrinsic radioactivity and the annihilation photons.

Curve	pC	keV	standard deviation [pC]
LYSO x-ray peak	15.04	55	5.439
LYSO γ line 1	51.08	202	15.58
LYSO γ line 2	78.16	307	14.52
^{68}Ga	118.2	511	5.856

perfectly linear. The energy calibration is also necessary for the determination of the energy resolution of the device and for the reconstruction of the Compton scattered events. The energy calibration must be performed channel by channel, in this preliminary work the calibration is performed for one crystal.
The position in charge units of the three peaks of the LYSO, calculated in Section 5.1, and the position in charge units of the photoelectric peak of the 511 keV photons, obtained in 5.2, are used for the energy calibration. The position, the relative energy and the relative error of each peak are again listed in Table 5.5. A linear fitting is applied to the LYSO peaks. The equation of the straight line that passes through the points is:

$$Q(E) = 2.2504 * E + 1.2487 \tag{5.3}$$

where the Q is the position of the peak in charge scale (pC) and E is the energy in keV. The coefficient of determination of this line is $R^2 = 1$. This result means the device has an optimal linear response at low energies. The point corresponding the 511 keV energy is not along this line, but it is located below it, as shown in Figure 5.3.

The reason why the photoelectric peak at 511 keV is not along the linear fitting, but below that, comes from the non linear response of the MPPC at high energies. This photodetector starts to saturate at energies close to the photoelectric peak, due to the limited number of pixels of the device and the high emission of light from the scintillator crystals. This causes a deviation from the linearity, which in this case is about 8%.
In order to obtain a non-linear energy calibration curve, the charge units (pC) vs energy scale (keV) is parametrized with a 3-parameters fitting function. The fitting function is thus considered with a decreasing exponential trend, because it describes the saturation of the charge emitted by the photodetector at high energies:

$$Q(E) = c_1 + a_1 * exp(b_1 * E). \tag{5.4}$$

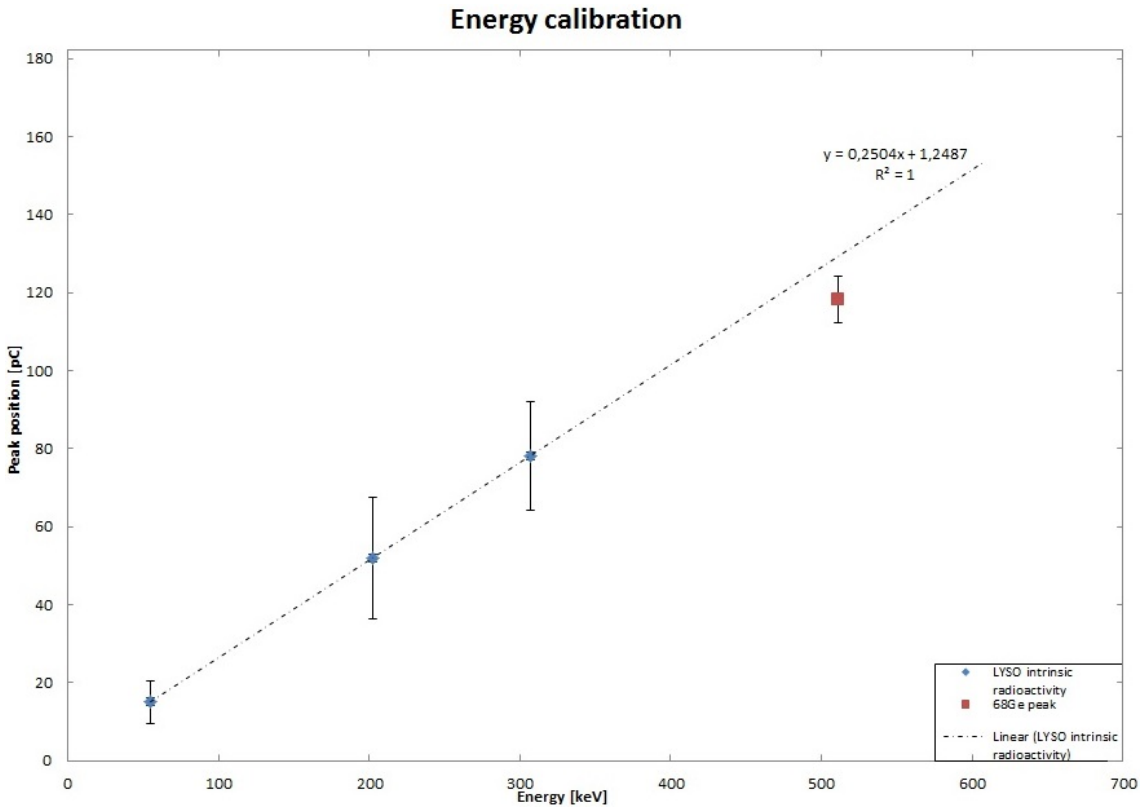

Figure 5.3: Linear fitting for the three LYSO peaks. The photoelectric peak at 511 keV is below this line because of the non linear response of the MPPC at high energies.

Table 5.6: Values of the parameteres of the 3-parametrized fitting function. The parameter b_1 is negative, because it describes the decreasing trend of the exponential fitting curve.

$\mathbf{a_1}$	-327.154
$\mathbf{b_1}$	-8.869×10^{-4}
$\mathbf{c_1}$	326.3476

Where Q is the charge unit and E is the energy. A dedicated MATLAB based code is used in order to evaluate the parameters (a_1, b_1 and c_1) and the coefficient of correlation, which results: $R^2 = 0.9996$. The values of these parameters are listed in the Table 5.6, the parameter b_1, that describes the trend of the exponential curve, is negative, as expected. The function obtained is plotted together with the linear fitting in Figure 5.4.

The non-linear fitting curve does not perfectly go straight on the linear curve at low energies. This equation for the fit is taken from AX-PET, where the deviation from the linear curve was about 5%, in this job the deviation is higher (about 8%). A possible reason for this difference arises from the relatively large errors (standard deviation) on the position of the mean values of the peaks of the intrinsic radioactivity. The curve nevertheless fits the points in agreement with the errors, as a matter of fact the high value of R^2 indicates the evaluated function fits the data well.

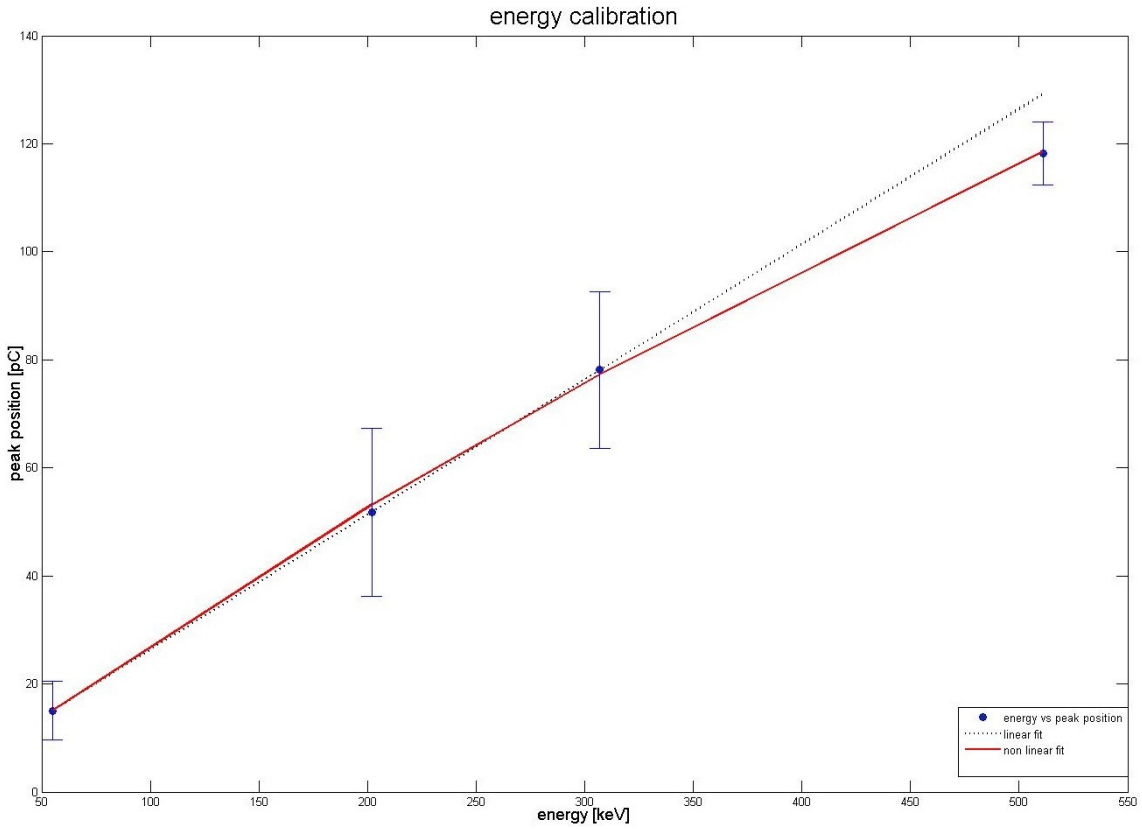

Figure 5.4: Energy calibration curve of one of the LYSO crystals (continuous line), which deviates from the linear fitting of the three LYSO peaks (dashed line).

With the inverse of the non-linear fitting curve the spectrum of the ^{68}Ga is converted in energy scale. The equation is again calculated with the MATLAB code and results being:

$$E(Q) = \frac{1}{b_1} * log\left(\frac{Q - c_1}{b_1}\right) \tag{5.5}$$

with the same parameters a_1, b_1 and c_1 of before. This function can also be written with the same expression used in AX-PET [5], using three new parameters (p_0, p_1 and p_2:

$$E(Q) = p_0 - p_1 * log\left(1 - \frac{Q}{p_2}\right) \tag{5.6}$$

considering the following relations between the parameters:

$$a_1 = -p_2 * exp\left(\frac{p_o}{p_1}\right) \tag{5.7}$$

$$b_1 = -\frac{1}{p_1} \tag{5.8}$$

$$c_1 = -p_2 \tag{5.9}$$

$$\tag{5.10}$$

The converted spectrum is plotted in Figure 5.5.

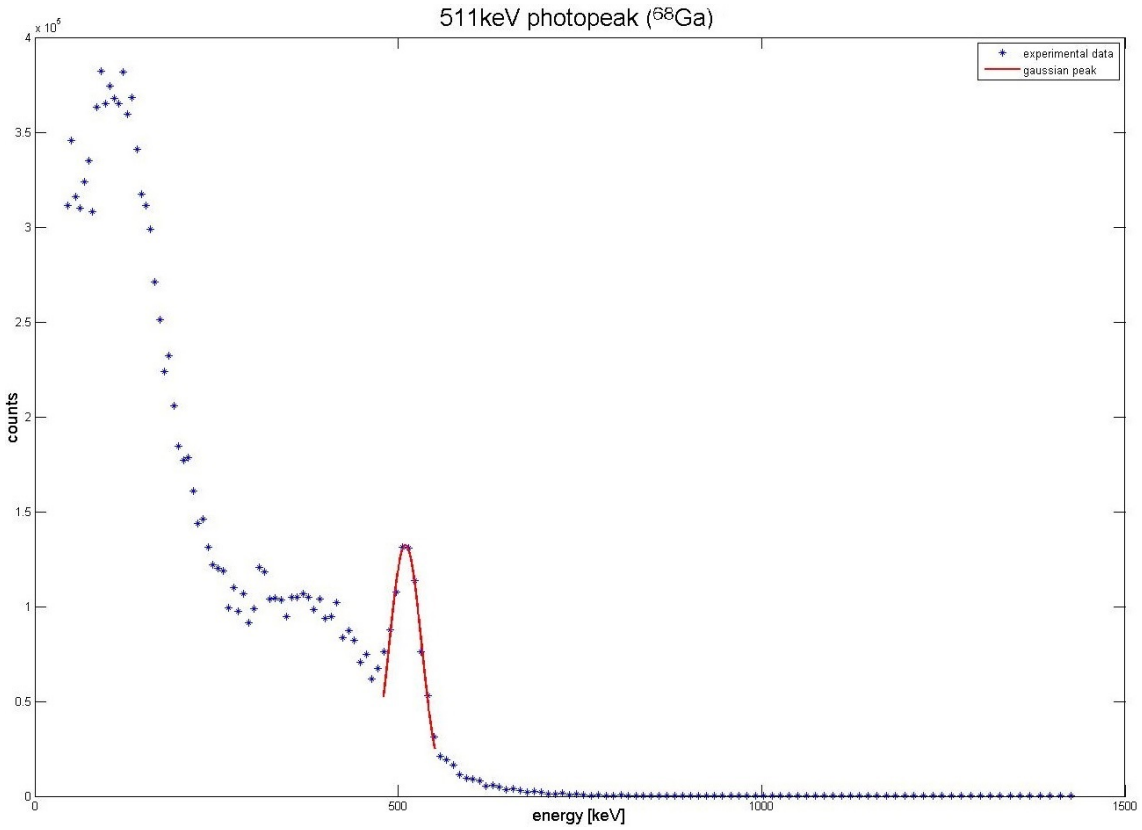

Figure 5.5: Spectrum of the 511 keV photons detected in one LYSO crystal, with a Gaussian fit for the photoelectric peak, in energy scale.

With a new Gaussian fit the position in energy of the photoelectric peak is estimated, together with its height and its standard deviation. The equation of the Gaussian fitting curve is again:

$$f(E) = a_2 * \exp\left(-\frac{E - b_2}{c_2}\right)^2 \tag{5.11}$$

Where the independent variable E is now the energy in keV. The parameter a_2 is the height of the peak of the curve, b_2 is the position of the centre of the peak, c_2 is the standard deviation and R^2 is the correlation coefficient. The values are listed in Table 5.7.

The position of the peak is given by the mean value of the Gaussian curve: $b_2 = 511$

Table 5.7: Parameters of the Gaussian fit curve for the photoelectric peak, converted in energy scale. The parameter a_2 is the height of the peak of the curve, b_2 is the position of the centre of the peak, and c_2 is the standard deviation and R^2 is the correlation coefficient.

Parameters of the Gaussian fit curve				
	a_2 [counts]	b_2 [pC]	c_2 [pC]	R^2
gaussian fit	1.324e+005	511	31.08	0.9718

keV, as expected. The peak is however not a perfect narrow line, it has indeed a width, given by the standard deviation c_2. Reasons for the widening and the uncertainty of the peak can be:

- dark noise and leakage from the electronic apparatus. The MPPCs and the electronic response can be affected by fluctuations due to the temperature and statistical errors that cannot be eliminated;
- scattered photons that interact with the surrounding material before impacting the scintillating bar.

These effects contribute to deteriorate the energy resolution of the device, causing the enlargement of the peak and the resulting error.

5.4 Energy resolution

The energy resolution defines the capability of the device to distinguish different energies in the spectrum. For a PET system the most important resolution is the one around the 511 keV. For this reason, although this is not the purpose of this thesis, a preliminary estimation of the energy resolution is calculated, staring from the spectrum extracted in section 5.3.
The energy resolution R is defined as:

$$R = \frac{FWHM}{X_0} \tag{5.12}$$

where X_0 is the amplitude of the peak and the FWHM is the full width at half maximum of it. The relation between the FWHM and the standard deviation σ of the Gaussian peak is defined as:

$$FWHM = 2\sigma\sqrt{2ln(2)} \simeq 2.355\sigma \tag{5.13}$$

According to the parameters in Table 5.7 the standard deviation is given by the parameter c_2: σ=31.08. The energy resolution at 511 keV is then:

$$R = \frac{FWHM}{X_0} = \frac{2.355 * 31.08}{511} \simeq 14\%. \tag{5.14}$$

This result is in line with the one obtained by AX-PET group $(11, 7\%)$ [5], although is a bit higher. A high value of energy resolution indicates a low capacity to distinguish two close values of energy. For this reason the result obtained by AX-PET is a bit better than the first estimation calculated with the Avantomography demonstrator.

6. CONCLUSIONS AND OUTLOOK

In this thesis, we have presented the Avantomography demonstrator, which has been implemented and tested during this job. This demonstrator is a functioning prototype of the new concept of new small PET cameras, with high resolution and high sensitivity at the same time, unlike the standard total body PET cameras. The device consists in two identical small, light and compact modules, the design, the implementation and the characterization of the demonstrator derive from the AX-PET collaboration [5] ideas. The geometry is based on a novel block detector with long scintillator bars placed in the transaxial plane and orthogonal wavelength shifter strip arrays. Each scintillating crystal and each WLC is read by a novel type of Geiger mode avalanche photodiodes, used as photodetector. Thanks to this implementation the demonstrator will permit to estimate the depth of interaction of the annihilation photons inside the scintillating crystals, allowing to reach a high resolution and high sensitivity with small dimensions of the device itself. The final purpose of this Master thesis, after the construction of the device, was the characterization of the scintillating crystals in terms of energy calibration. The energy calibration must be performed channel by channel, in this preliminary work the calibration was performed for one crystal.
Two test has been performed for the acquisition of different spectra, in order to obtain the energy calibration curve, that fits four points at different values of energy. In this way it was possible to estimate the response of the scintillating crystal and the electronic for acquisition at low energies and at 511 keV, which is the typical working energy of a PET. The first test consisted in the measure of the intrinsic radioactivity of LYSO, which corresponds to a 3 gamma ray cascade of energies 307 keV, 202 keV and 88 keV. The 4 modules were placed all together in order to create one single block of 20 crystals. The measurement was therefore acquired from the central crystal, because it had the probability to absorb the highest number of photons. The probability of internal conversion of the 88 keV photons is very high, because of that it wasn't possible to measure them. The measured photons at low energy corresponded to the K_α and K_β lines of the Lutetium, with an energy of 55 keV. The probability of internal absorption of the remaining photons emitted for intrinsic radioactivity inside one crystal itself is instead very low. For this reason the measured energy distribution of intrinsic radioactivity of the crystal placed inside the matrix was mostly given by the photons emitted from the nearby crystals and corresponds to three peaks at 55 keV, 202 keV and 307 keV. The second test has

been performed at the Tampere University Hospital using a linear radioactive source of ^{68}Ge/^{68}Ga, normally used for quality tests in PET. The ^{68}Ga emits positron and then annihilation photons, therefore the considered energy was the photopeak at 511 keV. The source was placed in the center of the field of view of the demonstrator, in order to equally irradiate all the scintillating crystals. For each peak a Gaussian fit was calculated using a dedicate MATLAB code, in order to obtain the position in terms of collected charge (signal emitted by the photodetector) and the standard deviation. The position in charge units of the three peaks of the LYSO and the position in charge units of the photoelectric peak of the 511 keV photons were used for the energy calibration. The energy calibration curve was calculated in two steps. First a linear fitting was applied to the LYSO peaks. The coefficient of correlation of this line is $R^2 = 1$. This result means the device has an optimal linear response at low energies. The photopeak at 511 keV is not along the linear fitting, but below that. The possible reason of that comes from the non linear response of the MPPC at high energies. This photodetector starts to saturate at high energies, due to the limited number of pixels of the device and the high emission of light from the scintillator crystals. This causes a deviation from the linearity that was visible even at 511 keV. As second step, in order to obtain a non-linear energy calibration curve, the charge units (pC) vs energy scale (keV) was parametrized with a 3-parameters fitting function. The fitting function is thus considered with a decreasing exponential trend, in order to describe the saturation of the charge emitted by the photodetector at high energies. From the calculation the deviation from the linear fitting curve of the position of the point at 511 keV has been estimated of about 8%. In AX-PET the deviation at the same energy was about 5%. A possible reason for this difference arises from the relatively large errors (standard deviation) on the position of the mean values of the peaks of the LYSO intrinsic radioactivity obtained in this job. The curve nevertheless fits the points in agreement with the errors, as a matter of fact the high value of $R^2 = 0.9996$ indicates the evaluated function fits the data well. With the inverse of the non-linear fitting curve the spectrum of the ^{68}Ga was converted in energy scale. The position of the mean value of the Gaussian fit of the peak is at 511 keV, as expected. As further calculation a first preliminary value of the energy resolution has been extracted from the measurements and the energy calibration curve. The result was about 14%, whereas in AX-PET it was $11,8\%$. The results obtained are in line with the ones in literature, although the performance of the Avantomography device is lightly lower than AX-PET one. Dark noise, leakage from the electronic apparatus and scattered photons, that interact with the surrounding material before impacting the scintillating bar, can be the reasons for the widening and the uncertainty of the peak position. These effects cause the enlargement of the peak and the resulting error and they also contribute to deteriorate the energy resolution of the device.

We can be reasonably satisfied for the results obtained with this first version of the demonstrator, but we consider necessary some further structural improvement and some additional tests. It may be possible to enhance the design, increasing the number of scintillating bars and the number of WLS strips. A higher number of LYSO bars will have the effect of increasing the efficiency on revealing photons, and therefore it would be not just a better design but a better performance of the device as well. A higher number of WLS strips, that permits to cover the entire length of each scintillating bar, will allow in the future to obtain the information about the spatial coordinates of the point of interaction between the annihilation photon and the crystal. Thanks to this information the signal processing will give digital images with high resolution, high sensitivity and without parallax error. It would be also possible to implement a temperature monitoring system for the photodetectors. The gain of the MPPCs shows a strong temperature dependence, which can negatively influence the performance during long data acquisition periods or during scans with several runs. This system has been already designed during this job, but it can be implemented only after the implementation of a dedicated electronic of acquisition. Tests with different reflecting material at the end of the scintillating crystal and the WLS strips can be performed. Tests with different optical glues for crystals or strips and MPPCs matching can be execute too in order to find the materials which give the best performance to the device. Additional dedicated tests in terms of energy calibration, energy resolution and response uniformity, performed channel by channel, are necessary for the complete characterization of the LYSO crystal and the WLS strips. Measurements in terms of axial resolution, time resolution and detection efficiency are necessary for the characterization of the functionality of each module of the prototype. All this characterizations are necessary for the future signal processing, because without them it is not possible to remove the noise from the signal. The following step in the development of the demonstrator is the implementation of an external trigger and a coincidence set-up. That would permit the measure of the temporal coincidence of the arriving of couple of annihilation photons, fundamental for the PET imaging. The measure in temporal coincidence permit to discriminate the couples of annihilation photons from the scattered ones. In this way the noise and the uncertainty of the position of the energy peak can be eliminate directly during the acquisition of the data. If the error is then small, the resulting energy resolution will be high, than a smaller energy window can be considered and only the useful data for the signal processing can be collected.

BIBLIOGRAPHY

[1] 3M^{TM} Optical Systems. Optically Clear Adhesives 8171CL - 8172CL. *http://solutions.3m.com*, February 2010.

[2] 3M^{TM} Optical Systems. Vikuiti^{TM} Enhanced Spectacular Reflector (ESR). *http://solutions.3m.com*, March 2013.

[3] Brian F. Aull, Andrew H. Loomis, Douglas J. Young, Richard M. Heinrichs, Bradley J. Felton, Peter J. Daniels, and Deborah J. L. Geiger-mode avalanche photodiodes for three-dimensional imaging. *Lincoln Laboratory Journal*, pages 335–350, 2002.

[4] P. Beltrame, E. Bolle, A. Braem, C. Casella, E. Chesi, N. Clinthorne, E. Cochran, R. De Leo, G. Dissertori, G. Djambazov, V. Fanti, K. Honscheid, S. Huh, I. Johnson, C. Joram, H. Kagan, W. Lustermann, F. Meddi, E. Nappi, F. Nessi-Tedaldi, J.F. Oliver, P. Pauss, M. Rafecas, D. Renker, A. Rudge, D. Schinzel, T. Schneider, J. Seguinot, S. Smith, P. Solevi, S. Stapnes, and P. Weilhammer. Construction and tests of demonstrator modules for a 3-D axial PET system for brain or small animal imaging. *Nuclear Instruments and Methods in Physics Research Section A: Accelerators, Spectrometers, Detectors and Associated Equipment*, 636(1, Supplement):S226 – S230, 2011.

[5] P. Beltrame, E. Bolle, A. Braem, C. Casella, E. Chesi, N. Clinthorne, R. De Leo, G. Dissertori, L. Djambazov, V. Fanti, M. Heller, C. Joram, H. Kagan, W. Lustermann, F. Meddi, E. Nappi, F. Nessi-Tedaldi, J.F. Oliver, F. Pauss, M. Rafecas, D. Renker, A. Rudge, D. Schinzel, T. Schneider, J. Séguinot, P. Solevi, S. Stapnes, and P. Weilhammer. The AX-PET demonstrator — Design, construction and characterization. *Nuclear Instruments and Methods in Physics Research Section A: Accelerators, Spectrometers, Detectors and Associated Equipment*, 654(1):546 – 559, 2011.

[6] SimonR. Cherry and Magnus Dahlbom. PET: Physics, instrumentation, and scanners. In Michael E. Phelps, editor, *PET*, pages 1–117. Springer New York, 2006.

[7] W. Chewpraditkul, L. Swiderski, M. Moszynski, T. Szczesniak, A. Syntfeld-Kazuch, C. Wanarak, and P. Limsuwan. Scintillation Properties of LuAG:Ce, YAG:Ce and LYSO:Ce Crystals for Gamma-Ray Detection. *Nuclear Science, IEEE Transactions on*, 56(6):3800 –3805, dec. 2009.

[8] Peter E Valk Dale L Bailey, David W Townsend and Michael N Maisey, editors. *Positron Emission Tomography*. Springer London, 2005.

[9] B. Dolgoshein, V. Balagura, P. Buzhan, M. Danilov, L. Filatov, E. Garutti, M. Groll, A. Ilyin, V. Kantserov, V. Kaplin, A. Karakash, F. Kayumov, S. Klemin, V. Korbel, H. Meyer, R. Mizuk, V. Morgunov, E. Novikov, P. Pakhlov, E. Popova, V. Rusinov, F. Sefkow, E. Tarkovsky, and I. Tikhomirov. Status report on silicon photomultiplier development and its applications. *Nuclear Instruments and Methods in Physics Research Section A: Accelerators, Spectrometers, Detectors and Associated Equipment*, 563(2):368 – 376, 2006.

[10] Eidgenoessische Tech. Hochschule Zuerich (CH). *AX-PET: Demonstration of a novel PET concept*. Chiara Casella, 2012.

[11] ELJEN Technology. EJ-260 plastic Scintillator. *www.eljentechnology.com*, March 2013.

[12] Epoxy Technology. EPO-TEK®EE129-4 Technical Data Sheet. *www.epotek.com*, 2013.

[13] Hamamatsu. MPPC®(Multi-Pixel Choton Counter) Technical Information. *www.hamamatsu.com*, March 2013.

[14] Paul Lecoq. New trends in PET detector developments. In Stefaan Tavernier, Alexander Gektin, Boris Grinyov, and WilliamW. Moses, editors, *Radiation Detectors for Medical Applications*, NATO Security through Science Series, pages 81–110. Springer Netherlands, 2006.

[15] Tom K. Lewellen. Time-of-flight PET. *Seminars in Nuclear Medicine*, 28(3):268 – 275, 1998. The Coming Age of PET (Part 1).

[16] SergiyS Makeyev. A look at medical imaging trends through the eyes of a medical doctor. In Stefaan Tavernier, Alexander Gektin, Boris Grinyov, and WilliamW. Moses, editors, *Radiation Detectors for Medical Applications*, NATO Security through Science Series, pages 1–13. Springer Netherlands, 2006.

[17] R.S. Miyaoka, T.K. Lewellen, H. Yu, and D.L. McDaniel. Design of a depth of interaction (DOI) PET detector module. *Nuclear Science, IEEE Transactions on*, 45(3):1069–1073, 1998.

[18] National Instrument. LabVIEW . *www.ni.com/labview*, 2013.

[19] J.M. Ollinger and J.A. Fessler. Positron-Emission Tomography. *Signal Processing Magazine, IEEE*, 14(1):43 –55, jan 1997.

[20] Gopal B. Saha. *Basics of PET Imaging*. Springer New York, 2010.

[21] Saint-Gobain Crystals. PreLude 420 Data Sheet. *www.detectors.saint-gobain.com*, March 2013.

[22] Michael E. Phelps Simon R. Cherry, James A. Sorenson. *Physics in Nuclear Medicine*. Elsevier Health Sciences, 2012.

[23] Vertilon. User Manual PhotoniQ Series IQSP480/IQSP482/IQSP580/IQSP582 Multi-Channel Data Acquisition Systems. *www.vertilon.com*, Feb 2011.

[24] Vertilon. IQSP582 PhotoniQ 64 Channel Data Acquisition System Product Sheet. *www.vertilon.com*, March 2013.

[25] Vertilon. SDS232 32 Channel SMB Distribution System Product Sheet. *www.vertilon.com*, March 2013.

[26] C.J. Zorn. A Study of Silicon Photomultiplier Sensor Prototypes for Readout of A Scintillating Fiber / Lead Sheet Barrel, Calorimeter . *Nuclear Science Symposium Conference Record, 2007. NSS '07. IEEE*, 2007.